JOURNAL OF PETROLOGY | VOLUME 54 | NUMBER 1 | PAGES 75–102 | 2013 | doi:10.1093/petrology/egs064

Magma Rheology Variations in Sheet Intrusions of the Ardnamurchan Central Complex (Scotland) Inferred from Gabbro Inclusion Characteristics

C. MAGEE[1,2]*, B. O'DRISCOLL[3,4], M. S. PETRONIS[5], C. T. E. STEVENSON[1], P. L. CLAY[6] AND R. GERTISSER[3]

[1]SCHOOL OF GEOGRAPHY, EARTH, AND ENVIRONMENTAL SCIENCES, UNIVERSITY OF BIRMINGHAM, BIRMINGHAM B15 2TT, UK

[2]DEPARTMENT OF EARTH SCIENCES AND ENGINEERING, IMPERIAL COLLEGE LONDON, LONDON SW7 2BP, UK

[3]SCHOOL OF PHYSICAL AND GEOGRAPHICAL SCIENCES, KEELE UNIVERSITY, KEELE ST5 5BG, UK

[4]SCHOOL OF GEOLOGICAL SCIENCES, UNIVERSITY COLLEGE DUBLIN, BELFIELD, DUBLIN 4, IRELAND

[5]ENVIRONMENTAL GEOLOGY, NATURAL RESOURCE MANAGEMENT DEPARTMENT, NEW MEXICO HIGHLANDS UNIVERSITY, PO BOX 9000, LAS VEGAS, NM 87701, USA

[6]SCHOOL OF EARTH, ATMOSPHERIC AND ENVIRONMENTAL SCIENCES, UNIVERSITY OF MANCHESTER, MANCHESTER M13 9PL, UK

RECEIVED FEBRUARY 23, 2011; ACCEPTED AUGUST 28, 2012
ADVANCE ACCESS PUBLICATION OCTOBER 13, 2012

Entrainment of xenoliths and their consequent assimilation are key processes in modifying the crystallization kinetics and magma dynamics of conduit systems. Here, an integrated textural and mineral chemical study of the evolution of a suite of gabbroic inclusions within a set of sheet intrusions from the Ardnamurchan Central Complex, NW Scotland, is presented. The key findings are as follows: (1) the host magma sheets and inclusions are not cognate; (2) there are microstructural and mineral chemical similarities between the gabbroic inclusions and the textures and mineralogy of the major Hypersthene Gabbro on Ardnamurchan; (3) orientations of magnetic fabrics within the host sheet groundmass and within the gabbroic inclusions are virtually identical. Field observations suggest that the inclusions were derived from the Hypersthene Gabbro and were entrained in a few laterally restricted magma segments that subsequently coalesced with inclusion-free segments into continuous sheets. Using Stokes' Law and adaptations thereof, we calculate that the magma within the inclusion-free segments behaved as a Newtonian fluid, with a potential settling velocity of $<0\cdot028\,\mathrm{m\,s^{-1}}$*. In contrast, the presence of gabbro inclusions probably modified the magma dynamics to Bingham-like behaviour. We infer that this variation in the magma rheology of separate segments continued after coalescence and internally partitioned the magma sheet, preventing lateral mixing and inclusion transport.*

KEY WORDS: *anisotropy of magnetic susceptibility; Ardnamurchan; magma rheology; inclusions; magma flow*

INTRODUCTION

Mafic magmas that feed and drive many volcanic systems are often compositionally modified during transport from the mantle and lower crust to the Earth's surface (Anderson, 1976; Huppert & Sparks, 1985; Sparks & Marshall, 1986; Blake & Fink, 2000; Polacci *et al.*, 2001; Rutherford, 2008; Genareau & Clarke, 2010). This can occur by processes that include magma mixing, assimilation of magma chamber crystal mushes and incorporation of conduit

---

*Corresponding author. Present address: Department of Earth Sciences and Engineering, Imperial College London, London SW7 2BP, UK. Telephone: +44 (0)20 7594 9983, E-mail: cmagee@imperial.ac.uk

wall-rock material. The crystallization kinetics of these magmas, which can be significantly altered by these processes, partially controls the viscosity and flow regime of the magma and thus potentially affects the ascent and eruption style (Melnik & Sparks, 1999; Rutherford, 2008). However, it has proved exceedingly difficult to quantify or even recognize the degrees of mixing and assimilation that have occurred in mafic magmas by studying the eruptive products alone (e.g. Humphreys *et al.*, 2009). Sub-volcanic sheet intrusions, such as dykes and sills, can provide an unparalleled perspective of these processes by freezing the intruding magma 'in transit', together with its associated crystal and inclusion cargoes. For example, Holness *et al.* (2007) studied gabbroic and peridotitic xenoliths entrained in Icelandic lavas and found that the original solidification microstructure of the crystal mushes was preserved to a significant degree, and Hrouda *et al.* (1999) outlined processes by which coaxial magmatic fabrics developed synchronously in xenoliths and the host magma. Other studies have highlighted how mechanical disaggregation of inclusions and incorporation into the host may be wholesale (e.g. Humphreys *et al.*, 2009) or how factors such as a rigid crystal framework may act to limit the degree to which inclusions (enclaves) mix with the host magma (Martin *et al.*, 2006). Analysing the impact of these processes on magma rheology therefore provides an opportunity to refine our knowledge of magma emplacement.

In this study, we report the results of integrated rock magnetic, quantitative textural and mineral chemical analyses of a suite of gabbro inclusions entrained in several closely spaced sheet intrusions from the southern part of the Ardnamurchan Central Complex in NW Scotland (Fig. 1) to assess the provenance of the inclusions, inclusion–host magma relationships and the transport mechanics of the system. Within the sheets themselves the gabbro inclusions are often restricted to one or two segments that extend <10 m along strike and are bounded by intrusive steps and/or broken bridges. To the best of our knowledge, these gabbro inclusions, and similar anorthositic inclusion-bearing sheets at Glebe Hill (Fig. 1a; Day, 1989), are unique on Ardnamurchan in terms of their spatial occurrence and petrography. From the complex cross-cutting relationships, the sheet intrusions studied here have been interpreted as spanning a significant proportion of the lifetime of the Ardnamurchan Central Complex (Richey & Thomas, 1930). Richey & Thomas (1930) briefly described these inclusions and suggested that they represent parts of intrusive sheets that were subsequently fragmented and disrupted by the current sheet lithology that utilized the pre-existing pathway during magma ascent. We disagree with this interpretation as the inclusions are gabbroic, with a well-developed cumulate texture, similar to that of the nearby (<1 km) Hypersthene Gabbro. We propose here that the inclusions were entrained from a partially solidified magma reservoir at depth. The inclusions preserve information on the fluid dynamics of the conduit systems, suggesting that the magma rheology of inclusion-bearing segments changed from Newtonian to Binghamian upon entrainment. These potential internal variations in magma rheology, between segments containing inclusions and those without, possibly partitioned the coalesced sheets and prevented lateral mixing of magma or inclusions.

GEOLOGICAL SETTING

The Ardnamurchan Central Complex, NW Scotland, represents the eroded roots of an ancient volcanic complex (Fig. 1a). It is one of the classic sub-volcanic central complexes of the British Palaeogene Igneous Province (BPIP) and was emplaced during the early stages of opening of the North Atlantic. In most cases, the BPIP central complexes intruded following the eruption of extensive basaltic lava fields onto Proterozoic metasedimentary rocks and Mesozoic strata in the Palaeocene (~60–58 Ma; Emeleus & Bell, 2005). Ardnamurchan, along with other BPIP centres (e.g. Mull and Skye), has been cited as an example of a system in which migrating volcanic centres developed throughout the lifetime of the complex (Richey & Thomas, 1930; England, 1988; Emeleus & Bell, 2005). In the case of Ardnamurchan, three centres (1, 2 and 3, in order of decreasing age) have been recognized from intrusive cross-cutting relationships and the foci of several cone sheet swarms (Fig. 1; Richey & Thomas, 1930), hereafter referred to as inclined sheets to avoid implied genetic connotations (Gautneb *et al.*, 1989). Centre 1 is considered to largely comprise numerous minor mafic intrusions (e.g. the Ben Hiant Dolerite) and volcaniclastic rocks (Richey & Thomas, 1930; Brown & Bell, 2007). Centre 2 consists of large gabbro intrusions of variable geometries, including laccoliths (i.e. the Hypersthene Gabbro) and ring dykes (Richey & Thomas, 1930; Day, 1989; Emeleus & Bell, 2005). The Hypersthene Gabbro is the closest major intrusion to the sheets studied here and can be divided into numerous geochemically and texturally distinct petrological facies that include the main olivine-bearing hypersthene gabbro, a subordinate augite-troctolite, olivine-rich gabbros and various quartz gabbros (Wells, 1953; Day, 1989). Centre 3 is principally composed of one large gabbro lopolith (i.e. the Great Eucrite; O'Driscoll *et al.*, 2006). However, the validity of these three centres has recently been questioned by Magee *et al.* (2012*a*,*b*), who have suggested that the majority of the inclined sheets and the Ben Hiant Dolerite may have originated from a source external to the Ardnamurchan Central Complex.

The gabbro inclusions of interest here occur in a localized set of mafic sheet intrusions, with variable geometries, along a 500 m coastal section on the southwestern

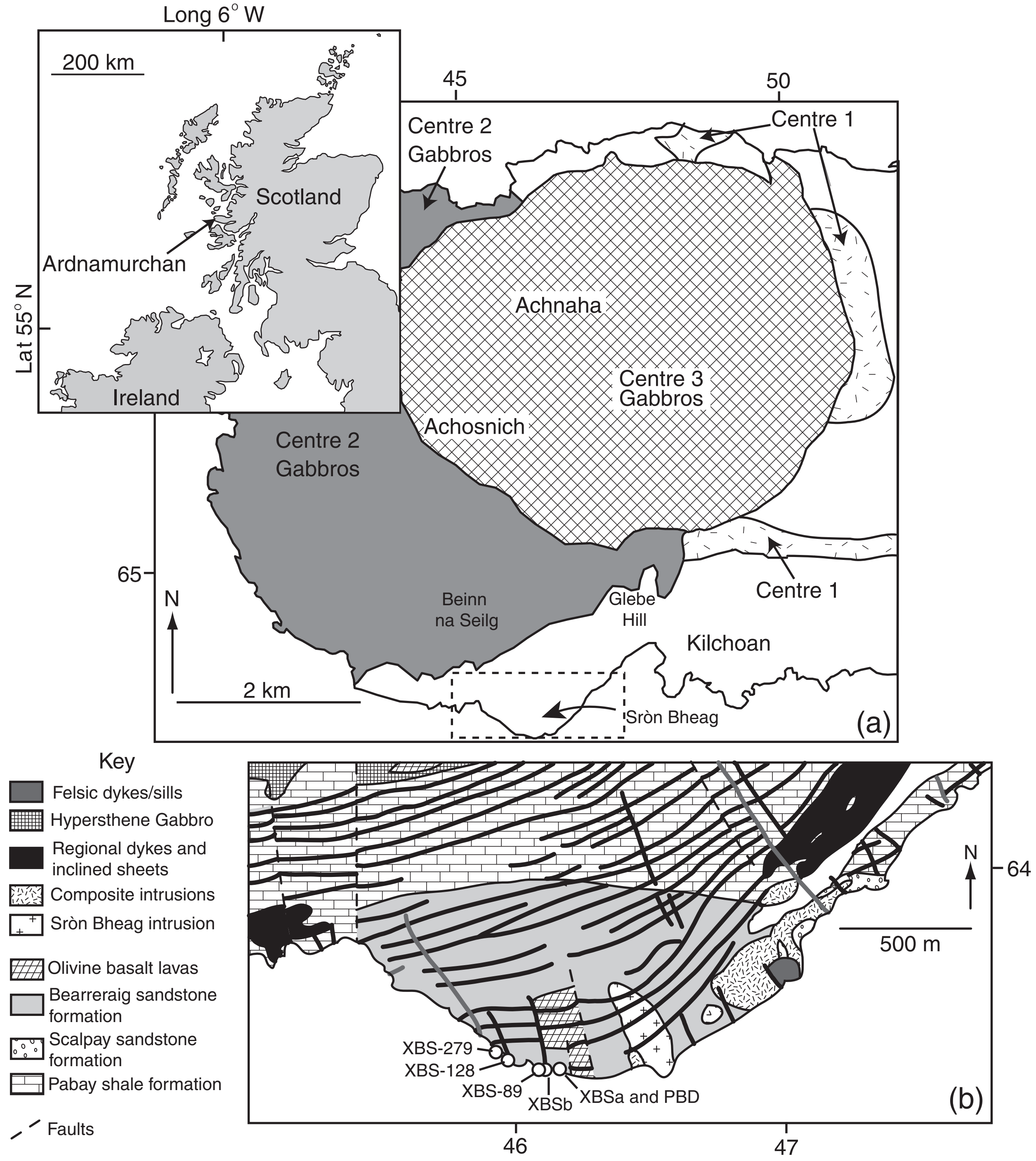

Fig. 1. (a) Map of the general geology of western Ardnamurchan (after Emeleus & Bell, 2005) and the location of the Sròn Bheag headland (inset shows the location of the Ardnamurchan peninsula in NW Scotland). The grid lines on the main figure are those of the UK National Grid. (b) Detailed geology of the Sròn Bheag area, highlighted in (a), including the studied sheet intrusion locations (after Emeleus, 2010).

shores of Ardnamurchan close to Sròn Bheag (NM 46178 62303, UK National Grid; Fig. 1b). Richey & Thomas (1930, pp. 348–349) noted that this area showed useful age relations between sheet intrusions and the host-rock lithologies they intrude, which include Middle Jurassic sedimentary rocks (i.e. Bearreraig Sandstone Formation) and Palaeogene olivine basalt lavas. Bedding in the Jurassic sandstone dips outward (southward) away from the Ardnamurchan Central Complex at ≥20°, attributed to early intrusion-induced doming (Richey & Thomas, 1930; Emeleus & Bell, 2005). The inclined sheets in this area typically strike east–west and dip ~40° N. A number of subvertical mafic dykes and inclined sheet intrusions, striking about north–south, also intrude the Bearreraig Sandstone Formation. North of this stretch of coastline (~1 km), the Jurassic sedimentary rocks (and sheet intrusions they contain) are observed to overlie a shallow southward-dipping contact (<15°) with the large Centre 2 Hypersthene Gabbro intrusion (Richey & Thomas, 1930), interpreted as a laccolith by Day (1989).

FIELD OBSERVATIONS AND PETROGRAPHY

Field observations

The field relations of the Sròn Bheag locality are illustrated here in detail in Figs 2–5 and on p. 348 of Richey & Thomas' (1930) Ardnamurchan Geological Survey memoir.

Porphyritic Basalt Dyke

In Fig. 2, a 1·5 m thick porphyritic basalt dyke (PBD) is intruded by the northern branch of a thin bifurcating (~70 cm) aphyric doleritic inclined sheet. The PBD is oriented 026/85° E and exhibits well-developed chilled margins against the Bearreraig Sandstone Formation (Fig. 3a). It is also characterized by the presence of large (≤5 cm in length), tabular, euhedral plagioclase crystals that show a substantial increase in grain size toward the core of the dyke. Clinopyroxene phenocrysts and scarce, small micro-gabbro inclusions (up to 10 cm in diameter with ~1 mm grain size) are observed in the PBD. Approximately 25 cm inside either margin of the PBD, strong contact-parallel planar fabrics are defined by tabular plagioclase crystals (Fig. 3a). Synneusis and imbrication of euhedral plagioclase phenocrysts are also observed within the core of the PBD. The largest crystals in the 50 cm thick core of the sheet show no alignment and a greater population density than toward either contact. At least three other similar porphyritic basalt dykes, oriented NW–SE, have been observed along the Ormsaigbeg to Mingary Pier coastline (NM 46965 62582 and NM 49255 62633, respectively) and in a road cutting NE of Ben Hiant (NM 54612 65106). Richey & Thomas (1930) identified these and other PBD-like intrusions, which they termed 'big-feldspar basalts', throughout Ardnamurchan. Similar basaltic blocks containing very coarse plagioclase phenocrysts are observed within the volcaniclastic deposits, suggesting that the porphyritic dykes were amongst the earliest intrusive phases of the Ardnamurchan Central Complex (Richey & Thomas, 1930). This is supported by field relationships, which reveal that the PBD-type dykes are cross-cut by Centre 1 and Outer Centre 2 inclined sheets (Richey & Thomas, 1930).

Inclusion-bearing sheet, XBSa

Both the inclined sheet and PBD are intruded by a 1 m thick basalt sheet (XBSa) oriented at 005/65° W and containing numerous gabbro inclusions (Fig. 2). This orientation changes to 008/28° W as the XBSa cuts the stratigraphy higher in the section. The north–south strike of the sheet is distinct from the local east–west strike of the inclined sheets. Chilled margins are developed except where XBSa is in contact with the PBD. The ~1 m offset of the PBD may be accounted for by the dilatational opening of XBSa (Fig. 2). North of the point where both sheets intersect, the XBSa contains locally abundant (≤75% of the dyke volume) coarse-grained (>5 mm) plagioclase-rich gabbro inclusions (Fig. 3b and c) that exhibit a cumulus (framework) crystalline texture. Within the gabbro inclusions the interstitial component increases towards the contact with the host groundmass and appears to be dominated by basalt similar in mineralogy and texture to the XBSa groundmass. The contacts of the gabbroic inclusions with the XBSa groundmass are diffuse and irregular, with transfer of single (or 'clots' of) plagioclase crystals from the gabbro inclusions into the dyke groundmass (Fig. 3c) being a common feature. Gabbro inclusions reach a maximum diameter of 75 cm (almost 75% the width of the sheet itself) with an average size of 40 cm. South of the intersection with the PBD, the XBSa contains no gabbro inclusions (Richey & Thomas, 1930) and displays a coarser-grained groundmass compared with the north of the intersection and also contains a broken bridge of thermally metamorphosed sandstone. These observations suggest that the exposed part of the XBSa may represent at least two separate sheet segments, with slightly variable crystallization histories, that coalesced upon dyke inflation (Hutton, 2009).

Inclusion-bearing sheet, XBSb

About 130 m farther west along the coast (Fig. 1, NM 4630 6222) another inclusion-bearing sheet (XBSb), oriented 002/90° and 1·5 m thick, forms a prominent dyke exposure in the cliff face (Fig. 3f). The large, coarse-grained gabbro inclusions exposed in this dyke are very similar in grain size and texture to those in the XBSa. The inclusions have an apparently random distribution; some areas of the dyke outcrop have a marked paucity of these inclusions, whereas others have an abundance. There is no apparent preference for inclusions to be concentrated at the margins or core of the XBSb. As with the XBSa, the inclusions in the XBSb are plagioclase-rich with cumulate textures and have diffuse boundaries with the dyke groundmass.

Inclusion-bearing sheet, XBS-89

Twenty metres west of the XBSb, three adjacent moderately inclined sheets ranging from 1·5 to 2 m in thickness crop out (Fig. 4a). These sheets have chilled upper and

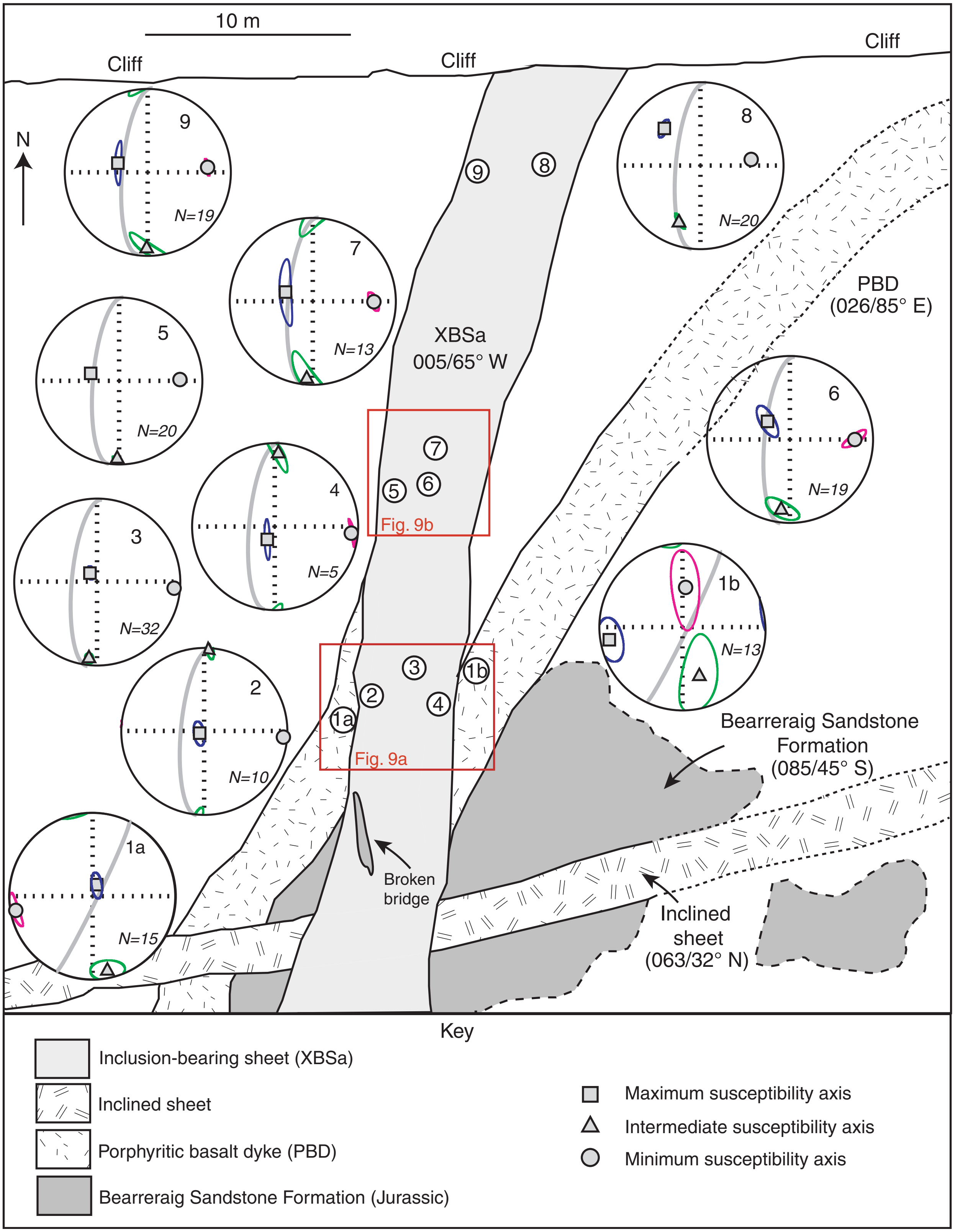

Fig. 2. Plan view of the field relations and AMS data for PBD and XBSa. On the equal-area, lower-hemisphere stereographic projections the great circles (grey) represent the plane of intrusion. For each principal susceptibility axis, 95% confidence ellipses are also plotted, although for some axes the confidence ellipses are smaller than the axis symbol. The circled numbers highlight the sample positions.

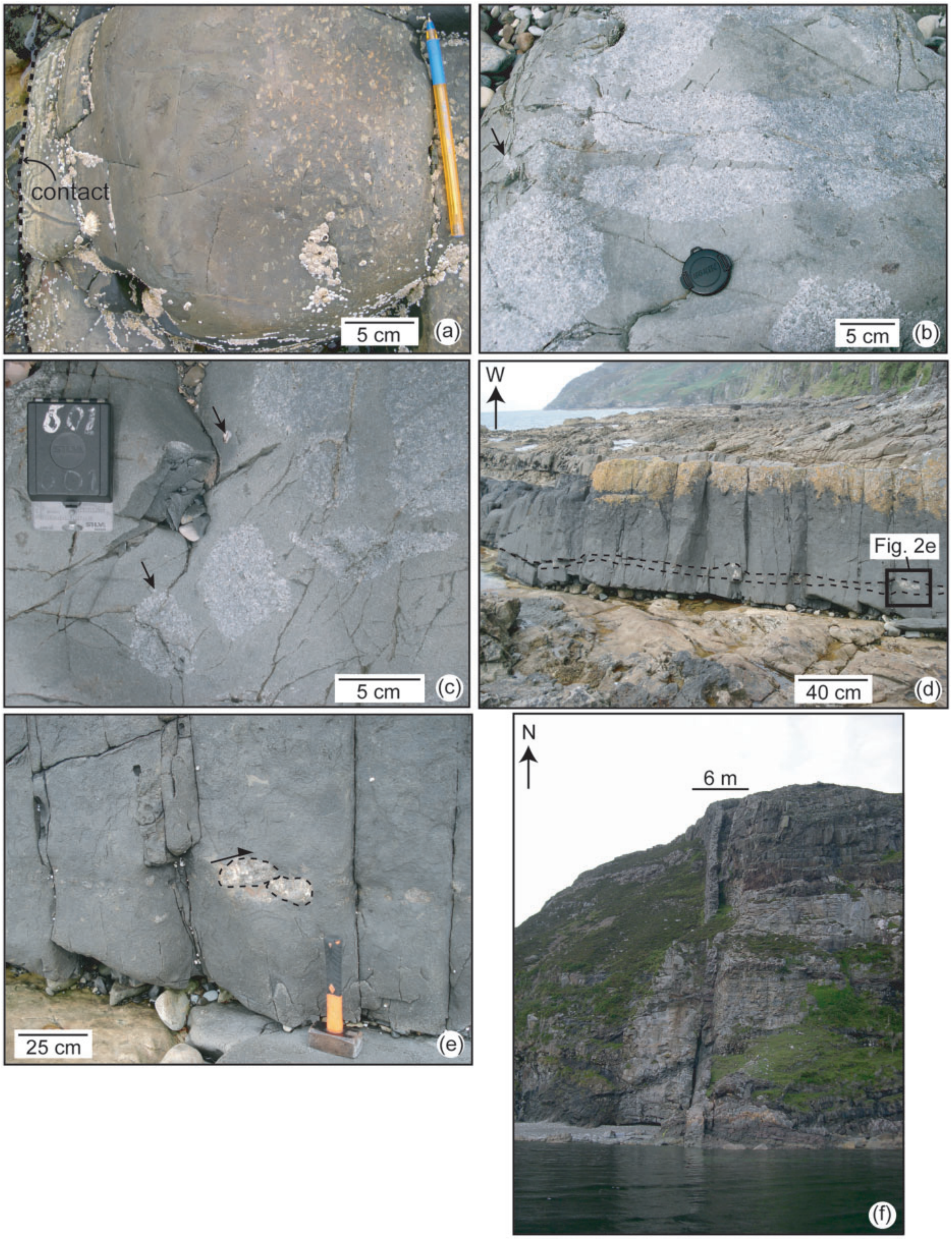

Fig. 3. Field photographs. (a) Chilled margin to the porphyritic basalt dyke (PBD; the contact with metasediment is towards the left of the image). (b, c) Irregular-shaped blocks in the XBSa. The intricate margins on the gabbro block in the bottom right of (b), suggesting reaction with melt, should be noted. Black arrows highlight single plagioclase crystals or glomerocrysts incorporated into the host sheet groundmass from the adjacent gabbro inclusions. (d) XBS-89 with zone of gabbro xenoliths highlighted in black. (e) Imbrication of gabbro clots in XBS-89. (f) Exposure of XBSb in the southern facing cliffs of Sròn Bheag. This dyke is ~2 m in width.

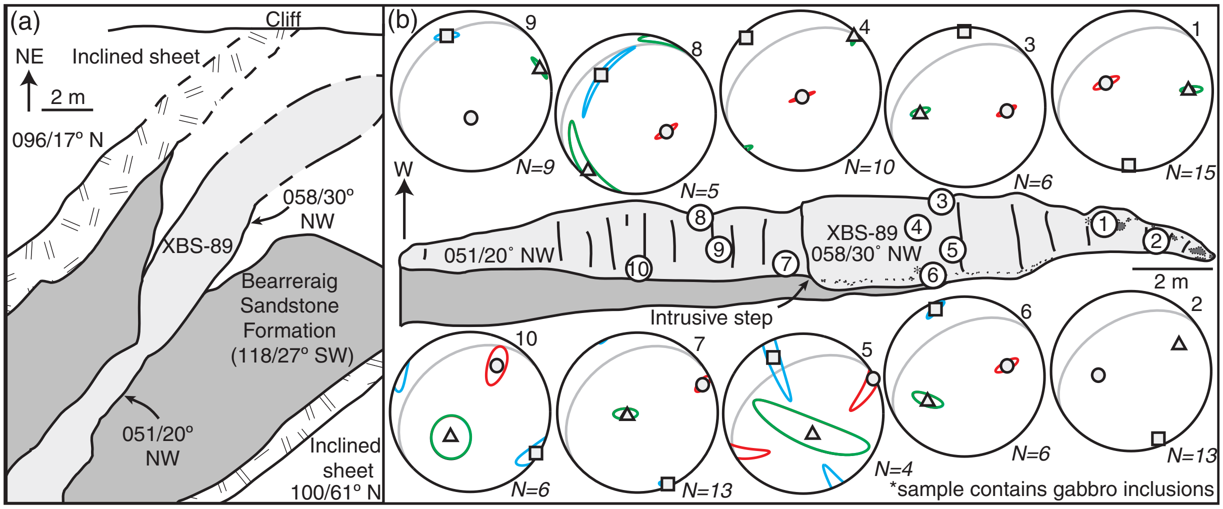

Fig. 4. (a) Plan view of field relations and AMS data for XBS-89 and nearby inclined sheets. The unornamented area is unexposed. (b) Cross-section view of XBS-89 highlighting the AMS results and sample positions. Key as in Fig. 2.

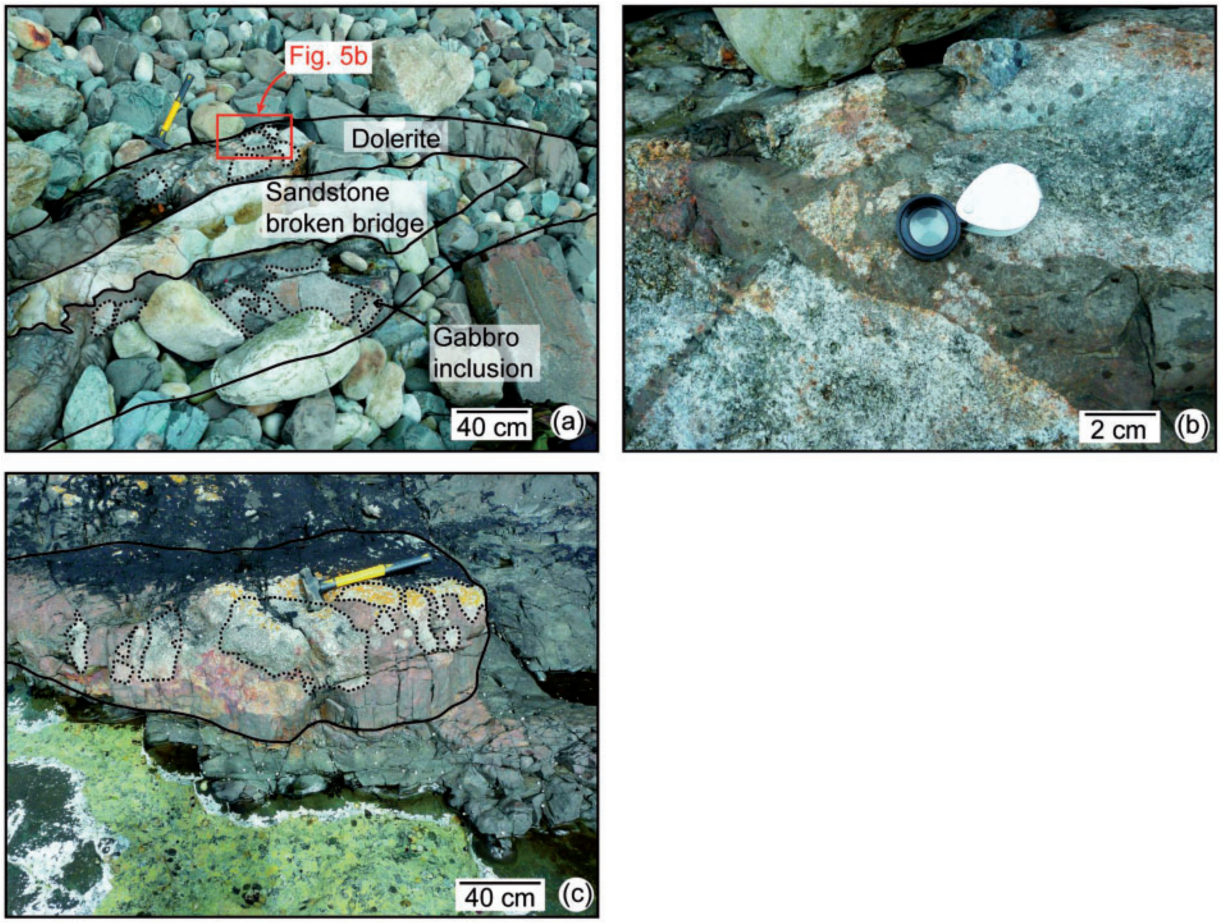

Fig. 5. (a) Accumulation of gabbroic inclusions around a thermally metamorphosed sandstone broken bridge in XBS-128. (b) Disaggregation of single and 'clots of' plagioclase crystals at the contacts of the inclusions in XBS-128. (c) Gabbroic inclusions highlighted in XBS-279.

lower margins. The middle sheet (XBS-89), oriented 055/25° NW, is the thickest of the three (~2 m) and contains a suite of plagioclase-rich cumulate inclusions, with a somewhat finer grain size (<3 mm) than those described above. These are mostly evenly distributed ~20 cm above the bottom contact of the sheet within a ≤15 cm thick planar zone (022/20 NW°) (Fig. 3d and 4b). The inclusions within this zone are typically 5 cm in diameter, with none greater than 15 cm observed. There is evidence of sporadic imbrication of these inclusions (Fig. 3e). Approaching the upper contact at the northern end of XBS-89, numerous randomly oriented gabbro inclusions are observed that range from 5 to 40 cm (Fig. 4b; e.g. samples 1 and 2). On the exposed upper surface of XBS-89, representing a plane ~10–20 cm below the eroded upper contact, numerous sandstone and basalt lava host-rock xenoliths (<40 cm) are encountered. No gabbro inclusions or host-rock xenoliths are observed to the south of a small intrusive step (Fig. 4b) that represents the point of coalescence between two originally separate sheet segments (Rickwood, 1990). The other two sheets are oriented 096/17° N and 100/61° N, consistent with the local inclined sheet trend contain no gabbro inclusions or host-rock xenoliths and have a coarser groundmass.

Inclusion-bearing sheets, XBS-128 and XBS-279

Farther west along the coast, two small intrusive basaltic sheets crop out that contain gabbro inclusions (XBS-128 at NM 45938 62397 and XBS-279 at NM 49500 64009; Fig. 1b). The thickness of both sheets is variable along strike but averages ~50 cm. An elongate broken bridge of sandstone is observed in XBS-128 (088/63 N) around which the gabbro inclusions are clustered (Fig. 5a). No additional inclusions are found along strike. Disaggregated single plagioclase crystals are also observed to have become entrained within the groundmass adjacent to the broken bridge (Fig. 5b). In XBS-279, oriented 074/43° N, the inclusions are also spatially restricted, although no associated structural feature (e.g. broken bridge) is observed (Fig. 5c). The inclusions of both sheets are similar in grain size and dimensions to XBS-89.

Petrography

Porphyritic Basalt Dyke

The plagioclase phenocrysts in the PBD are mostly euhedral and tabular. Micro-cracks are common in many crystals, the edges of which are frequently saussuritized and filled with quartz. Chemical zoning is common in many of the larger phenocrysts, but is partly to completely obscured in many instances by subsequent alteration of the plagioclase (Fig. 6a). The field observation that a synneusis texture is preserved by some plagioclase crystals is confirmed in thin section. The groundmass of the PBD hosts a population of randomly oriented plagioclase microlites (<0·1 mm) (Fig. 6a) that also exhibit micro-cracking and saussuritization. Close to the larger phenocrysts, the microlites are sometimes rotated into parallelism to the crystal edges, so that they appear to wrap the larger crystals. Abundant equigranular skeletal opaque crystals are present in the interstices of the microlite framework and have a maximum crystal size of 0·05 mm. Alteration textures of the PBD are evidenced by the greenish-coloured micaceous aggregates that are disseminated throughout the groundmass and that commonly fill subcircular olivine pseudomorphs of similar size (0·5–1 cm) to the plagioclase phenocrysts.

Inclusion-bearing sheets (XBSa, XBSb, XBS-89, XBS-128, and XBS-279)

The groundmass of the inclusion-bearing sheets (collectively XBS) is considerably fresher than that observed in the PBD. Skeletal clinopyroxene (<0·5 mm) and plagioclase microlites are abundant. The latter are more acicular, finer-grained (<0·05 mm) and less common than those observed in the PBD. Skeletal opaque crystals are common (up to 5 vol. %) in the groundmass of all XBS intrusions. Coarse-grained (~2 mm) cubic pyrite is abundant (up to 3 vol. %) in the XBS and minor amounts of pyrrhotite (<0·1 mm) are randomly disseminated throughout the groundmass.

In numerous thin-sections, the edges of the 'inclusions' are observed to comprise a uniform population of clots with touching crystal frameworks (30–60 vol. %) of relatively fresh medium- to coarse-grained plagioclase crystals (Fig. 6b), with average crystal sizes of 1–10 mm. The cumulus plagioclase crystals typically have a tabular, euhedral habit; crystal surfaces may be clean and straight or rounded and poorly defined if significant resorption has occurred (Fig. 6c). Pronounced oscillatory zoning and internal resorption surfaces in plagioclase crystals are common at inclusion edges, but not in plagioclase crystals toward the centres of inclusions (Fig. 6c and d). Petrographical observation confirms that the interiors of inclusions comprise more coherent coarse-grained gabbro. The interstitial areas between plagioclase crystals have a varied topology. In most instances around the edges of the inclusions, they are filled with the fine-grained inclusion-bearing sheet groundmass material (Fig. 6b). Some of the apparent dihedral angles subtended by the interstitial, cuspate groundmass-filled pockets and rounded cumulus plagioclase are 30–40°, suggesting an approach to melt-present textural equilibrium (Fig. 6b). Interstitial groundmass material may partially extend along the plagioclase–plagioclase grain boundaries (Fig. 6b). Toward the interiors of the inclusions, coarse-grained (up to 10 mm) intercumulus clinopyroxene oikocrysts enclosing cumulus plagioclase primocrysts become more frequent (≤15 vol. %; Fig. 6d) and little or no groundmass material is observed. Slightly higher (up to 60°) apparent dihedral angles are noted for plagioclase–plagioclase–clinopyroxene triple junctions

Fig. 6. Photomicrographs. (a) Chemical zoning of a cumulate plagioclase phenocryst within PBD. The randomly oriented plagioclase and clinopyroxene microlites at the bottom right should be noted. (b) Framework of tabular cumulus plagioclase within a gabbroic inclusion from XBSa. The pronounced chemical zoning of the middle plagioclase crystal and host magma groundmass along grain boundaries and at grain triple junctions should be noted (white arrows). (c) Complex resorption patterns within cumulus plagioclase crystals. The contact of the plagioclase with the host groundmass is irregular. (d) Clinopyroxene oikocryst (black) enclosing cumulus plagioclase. (e) Resorption texture exhibited in clinopyroxene within an inclusion of XBSa. Plagioclase–plagioclase–clinopyroxene triple junctions are also highlighted (black arrows). (f) Coarse clinopyroxene oikocryst in contact with the host groundmass and displaying evidence of resorption. All photomicrographs were taken with crossed polars.

(Fig. 6e), where intercumulus clinopyroxene is present. Intercumulus clinopyroxene crystals are rarely observed in contact with the groundmass (at the edges of inclusions), but in such cases are irregularly shaped and show evidence of significant resorption (Fig. 6e and f). Figure 6e also shows that irregular 'blebs' of the intercumulus clinopyroxene crystal continue into the groundmass (highlighted), separated in two dimensions from the main crystal, but still in optical continuity with it. This texture indicates localized resorption and dissolution of the inclusion clinopyroxene by the groundmass magma. Clinopyroxene crystals derived from the gabbro inclusions are not observed isolated in the groundmass.

PETROFABRIC ANALYSIS

Anisotropy of magnetic susceptibility (AMS) is a quantitative measure of the alignment of magnetic minerals in a rock (Tarling & Hrouda, 1993; Dunlop & Özdemir, 1997). It is particularly useful for fine-grained rocks (as in this study) where quantitative textural data (e.g. shape preferred orientation) are difficult to measure. In magnetite-bearing rocks (>0·1 vol. % magnetite), such as the basalt sheets studied here, the magnetic fabrics measured typically reflect the shape and/or distribution anisotropy of the magnetite petrofabric (Hargraves *et al.*, 1991; Tarling & Hrouda, 1993). When combined with detailed petrographic observation (e.g. shape preferred orientation), AMS fabrics have been shown to be a good indicator of the mineral petrofabric, which may record primary magma flow patterns in intrusive igneous rocks (e.g. King, 1966; Hrouda, 1982; Borradaile, 1987; Rochette *et al.*, 1992; Tarling & Hrouda, 1993; Cruden & Launeau, 1994; Archanjo *et al.*, 1995; Bouchez, 1997; Launeau & Cruden, 1998; Petronis *et al.*, 2004; Horsman *et al.*, 2005; O'Driscoll *et al.*, 2006, 2008; Stevenson *et al.*, 2007; Žák *et al.*, 2007). Samples for magnetic analyses were collected from the PBD, XBSa and XBS-89 intrusions (Table 1; Figs 2 and 4). Samples XBSa-7B, XBSa-7L, XBSa-9O, XBS-89.1 and XBS-89.6 are gabbroic inclusion samples that contain varying proportions of groundmass rock in the interstices of plagioclase crystals (i.e. 20–40 vol. %).

Rock magnetic experiments

A full characterization of the magnetic phase (or phases) that controls the AMS fabric is a very useful step in interpreting the AMS data. We conducted a suite of rock magnetic experiments at the New Mexico Highlands University (NMHU; USA) Paleomagnetic-Rock Magnetism Laboratory, on selected samples from the PBD (PBD-1L) and XBSa (XBSa-5H, XBSa-6A, XBSa-7B, XBSa-7L and XBSa-9O) to quantify the quantity and composition of mineral phase(s) contributing to the overall magnetic susceptibility. Rock magnetic experiments were also utilized to distinguish between single-domain (~<1 μm) and multidomain titanomagnetite (>100 μm) populations, an important distinction as single-domain titanomagnetites possibly produce magnetic fabrics inverse to the actual petrofabric (Potter & Stephenson, 1988; Hargraves *et al.*, 1991; Rochette *et al.*, 1992, 1999; Dragoni *et al.*, 1997; Aubourg *et al.*, 2002; Ferré, 2002; Cañón-Tapia & Chávez-Álvarez, 2004).

Low-field susceptibility versus temperature experiments

High-temperature, low-field susceptibility experiments were carried out in a stepwise heating and cooling fashion from 25°C to 700°C to 40°C in an argon atmosphere using an AGICO MFK1-A (multi-function kappabridge) susceptibility meter (operating at 900 Hz with a 200 $\mathrm{A\,m^{-1}}$ applied field) and a CS4 furnace attachment. These experiments allow for an evaluation of the magnetic mineral composition based on a Curie point estimate, the temperature at which a change in the magnetic behaviour of a grain occurs (Dunlop & Özdemir, 1997) within a given sample (Fig. 7). For magnetite, the Curie point is typically governed by the proportion of Ti (χ) in the crystal lattice. Low-temperature susceptibility measurements were conducted on an in-house built cryogenic measurement system and involved cooling samples to 77 K and measuring susceptibility every 18 s with the MFK1-A during warming to 298 K.

Lowrie–Fuller test

Experimental observations indicate that normalized alternating field (AF) demagnetization curves of weak-field thermoremanent magnetization (TRM) and strong-field TRM have different relationships for single-domain and multidomain grains of magnetite (Lowrie & Fuller, 1971; Dunlop & Özdemir, 1997). Following the modified Lowrie–Fuller test (Johnson *et al.*, 1975), the AF decay of normalized natural remanent magnetization (NRM; i.e. equivalent to a weak TRM in igneous rocks), anhysteretic remanent magnetization (ARM), and saturation remanence magnetization (SIRM; i.e. equivalent to a strong TRM) are compared. Laboratory investigations typically use weak-field ARM as a proxy for TRM, which we adhere to. Remanent magnetizations were measured on an AGICO JR6A dual-speed spinner magnetometer and demagnetization experiments were conducted using an ASC D-Tech 2000 AF demagnetizer.

IRM (isothermal remanent magnetization) acquisition curves

Isothermal remanent magnetization (IRM) acquisition experiments, employed to further delineate the domain state of magnetic phases, involved stepwise exposure to progressively stronger fields along the *z*-axis using a static impulse magnetic field, imparted by an in-house built static 3 Tesla impulse magnet, until saturation is obtained (SIRM). Backfield SIRM demagnetization to determine

Table 1: Anisotropy of magnetic susceptibility data

Sample	K_{mean}	K_1		K_2		K_3		P_j	T
	(10^{-3} SI)	Dec.	Inc.	Dec.	Inc.	Dec.	Inc.		
PBD-1a	02·96	0·21·00	79·00	169·00	09·00	260·00	06·00	1·03	0·17
PBD-1b	04·77	260·00	12·00	161·00	37·00	004·00	51·00	1·04	0·37
XBSa-2	77·70	242·00	84·00	004·00	03·00	094·00	05·00	1·11	0·52
XBSa-3	83·10	323·00	79·00	186·00	08·00	095·00	07·00	1·10	0·36
XBSa-4	69·10	210·00	75·00	003·00	13·00	094·00	07·00	1·10	0·43
XBSa-5	61·30	283·00	62·00	182·00	06·00	089·00	27·00	1·10	0·23
XBSa-6	78·00	309·00	62·00	184·00	07·00	090·00	27·00	1·10	0·35
XBSa-7*	03·51	288·00	62·00	184·00	07·00	090·00	27·00	1·04	0·58
XBSa-8	71·00	315·00	37·00	200·00	29·00	083·00	39·00	1·08	0·43
XBSa-9*	50·90	288·00	59·00	181·00	10·00	085·00	29·00	1·08	0·57
XBSa-89__1*	49·49	182·80	08·20	088·60	26·80	288·40	61·80	1·02	0·19
XBSa-89__2	43·82	157·10	03·90	265·20	77·60	066·30	11·70	1·02	0·51
XBSa-89__3	38·78	359·30	06·00	263·80	42·40	095·70	47·00	1·02	0·39
XBSa-89__4	31·65	314·20	05·70	044·50	03·10	162·60	83·50	1·04	0·21
XBSa-89__5	47·88	332·10	21·20	158·30	68·70	062·90	02·10	1·02	0·76
XBSa-89__6*	37·29	336·30	09·10	237·20	44·50	075·20	44·00	1·01	0·09
XBSa-89__7	36·34	158·00	10·10	061·60	32·20	263·20	55·90	1·02	0·27
XBSa-89__8	30·93	317·10	35·50	221·10	08·40	119·70	53·20	1·03	0·59
XBSa-89__9	20·93	335·00	24·50	069·90	10·60	181·40	63·00	1·03	0·54
XBSa-89__10	12·64	122·00	01·40	213·90	54·70	031·00	35·20	1·01	0·22

Dec. (declination) and Inc. (inclination) of magnetic susceptibility axes.
*Samples containing gabbroic inclusions.

the coercivity of remanence involved applying an increasing field along the negative *z*-axis until the positive *z*-axis magnetization was reduced to zero. Coercivity refers to the applied field intensity used to reduce a driven magnetic saturation back to zero (Dunlop & Özdemir, 1997).

Rock magnetic experiment results

The rock magnetic data indicate that the dominant magnetic mineral in all samples is a ferromagnetic (*sensu lato*) phase, probably multidomain low-Ti titanomagnetite. A small proportion of single-domain grain sizes was observed in XBSa-7L. These data suggest that the magnetic fabric in all of the samples examined is carried by titanomagnetite, with little to no contribution from the silicate mineral phases, and can be interpreted in a straightforward manner (see Rochette *et al.*, 1999; Ferré, 2002). Wider variability in magnetic mineralogy and titanomagnetite domain size within the gabbro inclusions, compared with the host sheet groundmass, is indicated by data from the XBSa samples collected from within the gabbroic inclusions. The raw rock magnetic data are provided as Supplementary Data in Electronic Appendix 1 (available for downloading at http://www.petrology.oxfordjournals.org).

Low-field susceptibility versus temperature experiments

Six samples of gabbroic inclusions and groundmass basalt from the PBD and XBSa yield a spectrum of results that vary from fully reversible curves with a single Curie point estimate to more complex irreversible curves with two or more inferred Curie point estimates (Fig. 7). On heating, XBSa-5H, XBSa-6A, and XBSa-9O monotonically increase in susceptibility with a strong increase in susceptibility at the Curie point at 566°C, 560°C and 566°C, respectively; consistent with a low-Ti ($\chi = 0{\cdot}027$, 0·037 and 0·027, respectively) titanomagnetite phase (Fig. 7). XBSa-7B shows an increase followed by a decrease (a 'bump') in susceptibility over the interval from 200°C to 350°C that is not present on the cooling curve. This is often interpreted to reflect the homogenization of two exsolved Fe–Ti oxide phases into a single titanomaghemite phase during the experiment (Fig. 7; Özdemir & O'Reilly, 1981, 1982), although this process is not well understood (Hrouda, 2003). On continued heating, susceptibility steadily increases with a pronounced peak and Curie point at 568°C, indicative of a low-Ti ($\chi = 0{\cdot}024$) titanomagnetite phase. XBSa-7L shows little dependence on heating up to about 500°C followed by an increase in susceptibility and

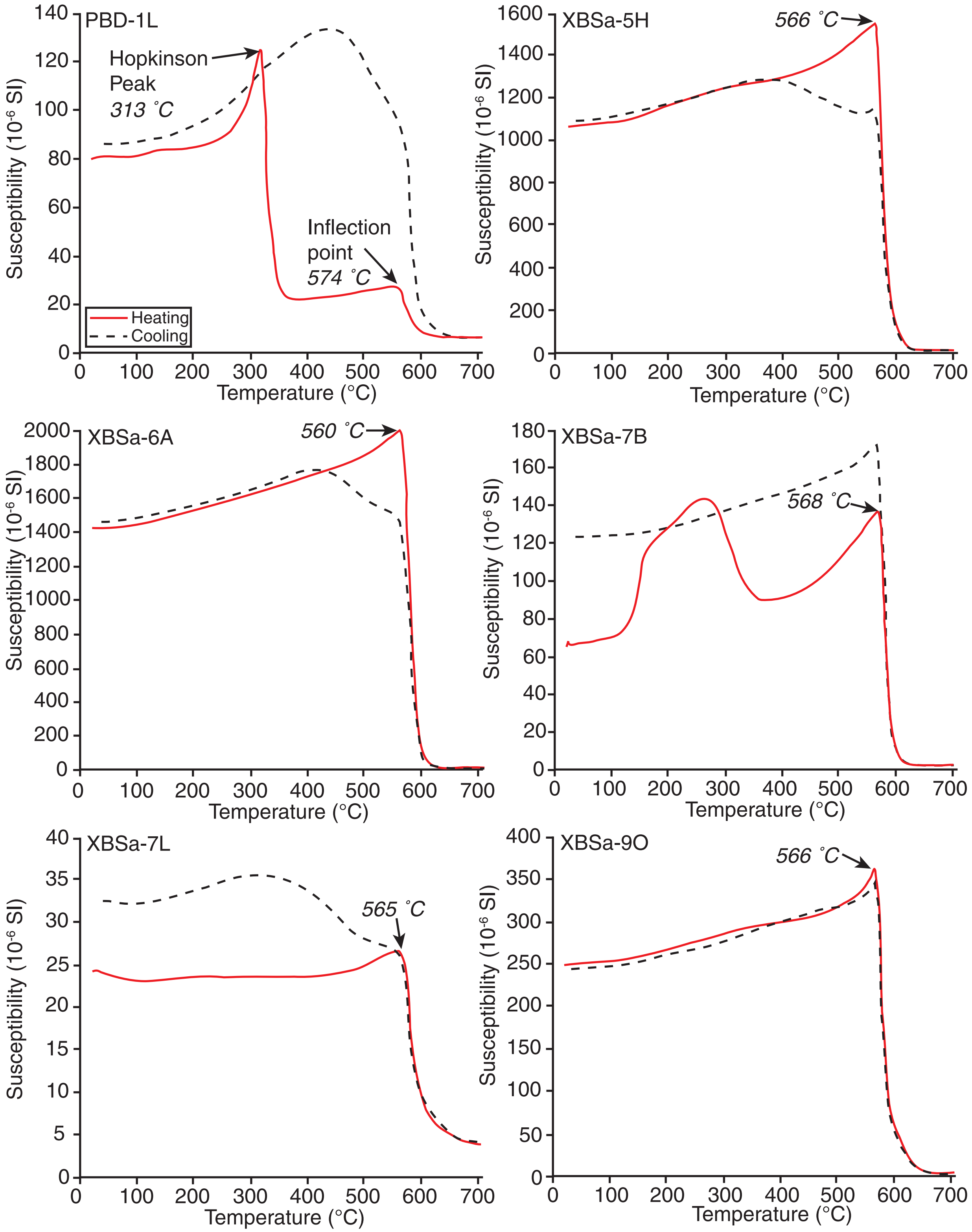

Fig. 7. Continuous susceptibility vs temperature experiments. Each Curie point estimate determined either by the Hopkinson peak (Moskowitz, 1981) or the inflection point method is indicated.

Curie point at 565°C (Fig. 7). The susceptibility on the cooling curve is greater than the room temperature susceptibility, which reflects the generation of a new magnetic phase (titanomagnetite) by low-temperature oxidation of a less magnetic phase (Irving, 1970; Marshall & Cox, 1972; Johnson & Atwater, 1977). PBD-1L yields a complex heating–cooling curve with two Curie points present on the heating curve and a behaviour that is difficult to interpret on the cooling curve (Fig. 7). It shows little dependence on heating up to about 275°C followed by a rapid increase in susceptibility with a pronounced peak and Curie point at 313°C; a temperature consistent with the presence of an Fe-sulphide phase, probably pyrrhotite. On further heating the susceptibility decreases rapidly to 25% of its room temperature value and shows little temperature dependence on heating. A second Curie point at 574°C is revealed by an abrupt drop in susceptibility over the interval between 560°C and 590°C and indicates low-Ti ($\chi = 0{\cdot}014$) titanomagnetite.

In the low-temperature magnetic susceptibility experiments only samples XBSa-5H and XBSa-6A exhibit an initial increase in susceptibility from −196°C to ~ −165°C, a typical behaviour of multidomain grains (Walz & Kronmüller, 1994; Moskowitz *et al.*, 1998). All samples show a modest decrease in susceptibility on warming from beyond −165°C, until −100°C to 0°C where there is little to no temperature dependence on warming (Fig. 8a). This suggests that a ferromagnetic (*sensu lato*) mineral phase, probably titanomagnetite, dominates the magnetic mineralogy and hence controls the AMS fabric.

Lowrie–Fuller test

Alternating field (AF) demagnetization of the NRM (natural remanent magnetization) of three samples from gabbroic inclusions of XBSa and one sample from PBD reveals coercivity spectra ranging from single-domain magnetite (XBSa-7L) of moderate coercivity to pseudo-single-domain magnetite (PBD-1L and XBSa-9O) of intermediate to low coercivity (Fig. 8b; Dunlop & Özdemir, 1997). The coercivity crudely reflects the median destructive field required to randomize one-half of the initial remanence, with low and medium coercivity characterized by median destructive fields of 15–20 mT and 25–40 mT, respectively (Dunlop & Özdemir, 1997). The NRM of XBSa-7B did not respond to AF demagnetization, indicating the presence of a high-coercivity phase such as haematite and/or fine-grained maghemite and pyrrhotite. In large multidomain grains, SIRM requires larger destructive fields than ARM to reach the same normalized level. PBD-1L, XBSa-7B, and XBSa-9O yield magnetite-dominated behaviour and curves that suggest multidomain grain size, whereas XBSa-7L yields magnetite-dominated behaviour with an ARM curve that is more resistant than SIRM, indicative of a single-domain to pseudo-single-domain grain size (Fig. 8b).

IRM (isothermal remanent magnetization) acquisition curves

The curves show a narrow spectrum of responses within each sample, yet are consistent with the above observations of considerable variation between samples within the sheets (Fig. 8c). The XBSa and PBD sheet samples reveal steep acquisition curves reaching saturation between 0·3 and 0·5 T that are indicative of a cubic mineral phase (e.g. magnetite). The acquisition curves are characteristic of multi- to pseudo-single-domain magnetite behaviour with some influence from higher-coercivity single-domain magnetite. Backfield IRM (i.e. coercivity of remanence) is the field that reduces the saturation isothermal remanence to zero (Dunlop & Özdemir, 1997). The curves for PBD-1L, XBSa-7L and XBSa-9O show a very narrow range of responses, with coercivity of remanence values less than 0·1 T (Fig. 8). In contrast, XBSa-7B shows a moderate range of response, with a coercivity of remanence value of ~0·25 T (Fig. 8c). These coercivity of remanence values are roughly equal to the field strength required to impart median IRM acquisition, indicating that the magnetic grains are non-interacting (Dunlop & Özdemir, 1997).

Anisotropy of magnetic susceptibility

In this study, AMS samples were collected in the field as oriented blocks (XBS-89) and oriented drill-cores (PBD and XBSa), the latter using a portable gasoline-powered drill with a non-magnetic diamond bit. All samples were oriented using a magnetic and (when possible) a sun compass. From the block samples drilled in the laboratory (Owens, 1994), 4–15 (typically nine) 2·2 cm × 2·5 cm right-cylindrical specimens were extracted. All drill cores were prepared into similar specimens, using a diamond-tipped, non-magnetic saw blade with up to four specimens per sample obtained. The AMS fabrics of these specimens were measured on an AGICO KLY-3S Kappabridge (an induction bridge that operates at a magnetic field of 300 A m^{-1} and a frequency of 875 Hz) at the University of Birmingham (UK).

Magnetic susceptibility differences in specimens were measured in three orthogonal planes and combined with the measurement of one axial susceptibility to define the susceptibility tensor. The magnetic susceptibility tensor, which may be pictured as an ellipsoid, comprises the three principal susceptibility magnitudes ($K_1 \geq K_2 \geq K_3$) and a corresponding set of three orthogonal principal axis directions. In the case of block samples, it is assumed that the block represents a homogeneous multi-normal population and within-block variability is characterized through calculation of the 95% confidence limits on direction and magnitude parameters (Jelínek, 1978; Owens, 2000). The magnitude parameters are usually reported in terms of ‘size’, ‘shape’ and ‘strength’ (or ellipticity) of the ellipsoid.

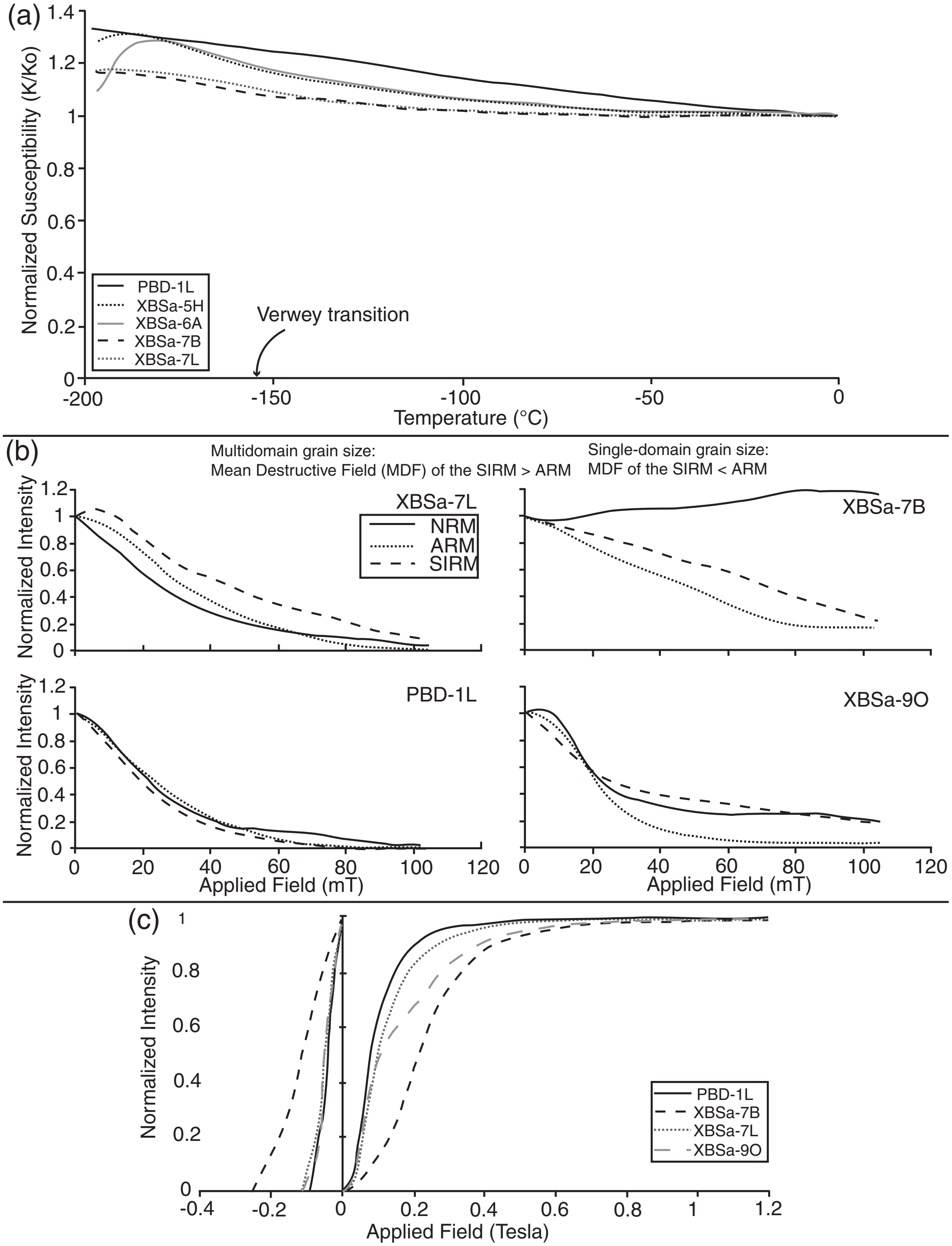

Fig. 8. (a) Low-temperature susceptibility experiments. Normalized reciprocal magnetic susceptibility (K/K_o) as a function of temperature. K, susceptibility at temperature T°C; K_o, susceptibility at 25°C. An ideal ferromagnetic curve would show no change in susceptibility with temperature; ideal paramagnetic curves are straight lines described by the Curie–Weiss law ($K_{para} = C/T - \theta$, where C is the Curie constant, θ is the paramagnetic Curie temperature, and T is temperature in Kelvin). The minor drop in susceptibility from 77 K in some samples is probably related to crossing the Verwey transition at ~120 K. (b) Modified Lowrie–Fuller test (Johnson *et al.*, 1975) comparing AF demagnetization response of natural remanent magnetization (NRM), anhysteretic remanent magnetization (ARM), and saturation isothermal remanent magnetization (SIRM). (c) Normalized isothermal remanent magnetization (IRM) acquisition and back-field IRM demagnetization curves for representative samples.

These include the mean (or bulk) susceptibility, $K_{\mathrm{mean}} = (K_1 + K_2 + K_3)/3$; the degree of anisotropy, P_{j} $(= \exp\sqrt{\{2[(\eta_1 - \eta)^2 + (\eta_2 - \eta)^2 + (\eta_3 - \eta)^2]\}})$, where $\eta = (\eta_1 + \eta_2 + \eta_3)/3$, $\eta_1 = \ln K_1$, $\eta_2 = \ln K_2$, $\eta_3 = \ln K_3$; Jelínek, 1978); and the shape parameter, T $\{= [2\ln(K_2/K_3)/(\ln(K_1/K_3)] - 1\}$. A value of $P_{\mathrm{j}} = 1$ describes a perfectly isotropic fabric, a P_{j} value of 1·15 describes a sample with 15% anisotropy, and so on. The quantitative measure of the shape of the susceptibility ellipsoid, T, ranges from perfectly oblate ($T = +1$) to perfectly prolate ($T = -1$). Further details on AMS theory and applications have been given by Khan (1962), Uyeda *et al.* (1963), Hrouda (1982), Tarling & Hrouda (1993), Bouchez (1997) and O'Driscoll *et al.* (2008).

Anisotropy of magnetic susceptibility results

The AMS fabric results are summarized in Figs 2, 4 and 9 and Table 1. K_{mean} values for the PBD are $\sim 3{\cdot}87 \times 10^{-3}$ SI, consistent with a titanomagnetite phase (in concentrations of 1–3 vol. %; Tarling & Hrouda, 1993). The XBSa samples confirm the petrographic observation that considerably more titanomagnetite (up to 5 vol. %) is present in the groundmass compared with PBD; the average K_{mean} here is $61{\cdot}83 \times 10^{-3}$ SI. For samples from the PBD and XBSa, P_{j} values are distributed between 1·03 and 1·11. The shape parameter T values indicate that the PBD samples have prolate AMS ellipsoids ($T = -0{\cdot}17$ to $-0{\cdot}37$), whereas all of the XBSa samples have moderately to strongly ($T = 0{\cdot}23$–$0{\cdot}57$) oblate ellipsoids. The data for XBS-89 reveal an average K_{mean} of $34{\cdot}98 \times 10^{-3}$ and P_{j} values of 1·01–1·04. The shape parameter T values for XBS-89 indicate that the AMS fabrics range from moderately prolate (−0·51) to moderately oblate (0·58). The fabrics are predominantly near-triaxial, tending towards prolate (−0·11 average).

The striking feature of most of the AMS orientations (except PBD-1 b and XBS-89.1) is that the magnetic lineations, regardless of ellipsoid shape, trend subparallel to the sheet dip azimuth (Figs 2, 4 and 9) irrespective of whether the samples measured are from the groundmass or from within the gabbroic inclusions. For example, XBS-89 has a sheet dip azimuth of 328° and the majority of K_1 lineations trend NW–SE (Table 1). In the PBD and XBSa, the K_1 lineations are generally steeply plunging (Figs 2 and 9), whereas in XBS-89 they are subhorizontal to gently plunging (Fig. 4). Although the magnetic foliations typically strike subparallel to the intrusion plane, there are several exceptions (PBD1b, XBS-89.1, XBS-89.2, XBS-89.5, XBS-89.6, XBS-89.7and XBS-89.10; Figs 2 and 9). In XBSa the AMS ellipsoids measured within the gabbro inclusions (XBSa-7) are more oblate and the K_{mean} ($3{\cdot}51 \times 10^{-3}$ SI) is an order of magnitude lower than that for the surrounding groundmass, but the same mean K_1 directions are observed (Fig. 9; Table. 1).

CRYSTAL SIZE DISTRIBUTION

Crystal size distribution (CSD) is a method of quantitatively analysing the number of crystals of a particular mineral per unit volume within a series of defined size intervals (Marsh, 1988, 1998; Higgins, 2000, 2006*a*) and is usually plotted as population density (logarithmic number of crystals per unit volume) against crystal size (maximum length). CSD analyses were carried out here principally on the PBD phenocryst, XBS gabbro inclusion and XBS-89 groundmass plagioclase populations to determine variabilities in their crystallization kinetics. Log–linear CSD profiles are often inferred to relate to the nucleation and growth of a single population of crystals (e.g. Cashman & Marsh, 1988; Resmini & Marsh, 1995; Marsh, 1998; Higgins, 2006*a*), whereas curvature in the CSD plot profiles is attributed to processes that occur post-nucleation (e.g. compaction, Boorman *et al.*, 2004; mixing of crystal populations, Jerram *et al.*, 2003; textural coarsening, Higgins, 2002). The approach taken in this study for CSD measurement has been described by Higgins (2000, 2006*b*) and involves digitizing 'texture maps' from both thin sections and polished hand-specimen slices for calculation of crystal long axes and other parameters (Table 1) using the image analysis software ImageJ. The smallest crystal sizes were measured in all CSDs except for the XBS-89 plagioclase microlites, for which only plagioclase crystals >0·1 mm were measured. Over 200 crystals were measured where available (Table 1). The CSD data were stereologically corrected following the methods of Higgins (2000) and the program CSDCorrections 1.37. CSDCorrections 1.37 was also used to calculate the goodness of fit (Q) values, which describe the CSD profile shape (i.e. log–linear or curved) (Higgins, 2006*a*). Characteristic lengths (Ci) were calculated to communicate the CSD slope as a length ($Ci = -1/\mathrm{slope}$) to allow for easier data comparison (Higgins, 2006*b*).

Crystal size distribution results

The CSD data are summarized in Table 2 and plotted in Fig. 10 (the raw data are available in Supplementary Data, Electronic Appendix 2). Goodness of fit (Q) values were calculated in CSDCorrections 1.37 and indicate that the majority of CSD profiles are log–linear ($Q > 0{\cdot}1$) whereas a few, notably the gabbroic inclusion CSD curves of XBS-89, are curved ($Q \ll 0{\cdot}1$) (Higgins, 2006*a*). A plot of Ci vs intercept (Fig. 10c) shows that the measured data fall below the calculated closure limits, verifying the results obtained (Higgins, 2006*b*). The CSD profile for the XBS-89 inclusion (1) shows a pronounced 'hump' at smaller size fractions (Fig. 10a), often interpreted as evidence of textural coarsening (Higgins, 2006*b*). No other profiles display a similar 'hump', although this may reflect the paucity of measurable smaller size fractions in other samples (Fig. 10a). The bulk of the CSD slopes for plagioclase

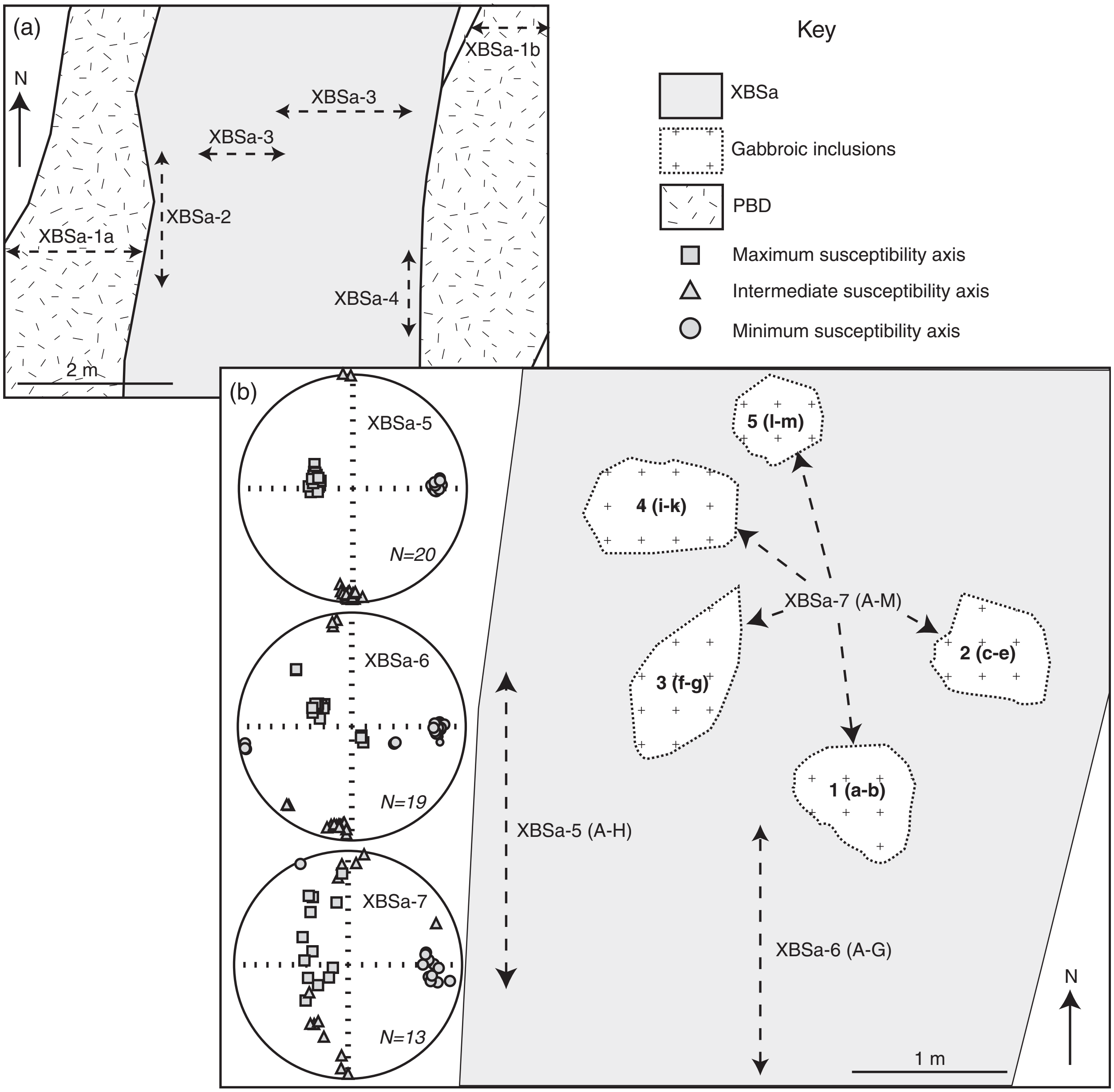

Fig. 9. (a) Sketch showing locations of samples collected across PBD and XBSa (see Fig. 3). (b) AMS data from part of XBSa showing that the five gabbro inclusions in the vicinity have virtually identical AMS fabrics to the groundmass in the core and at the margins.

grains in gabbro inclusions from XBSa, XBS-89, XBS-128 and XBS-279 are grouped in the range −0·93 to −1·52 mm^{-1} with intercepts of −0·60 to 2·16 mm^{-4} (Fig. 10d). The single CSD measured from the PBD has a slope that is shallower (−0·25 mm^{-1}) with a corresponding low intercept of −4·52 mm^{-4}, indicating a lower population density of much larger crystals (Fig. 10b and d). The greatest population density of plagioclase crystals and steepest slope (−3·97 mm^{-1}) is observed in the groundmass microlite population of XBS-89 (Fig. 10d). The CSD data thus suggest the presence of three distinctive crystal populations: the PBD phenocrysts, XBS cumulate plagioclase and the host sheet microlites. Importantly, all of the XBS inclusion plagioclase yield remarkably similar CSD profiles.

MINERAL CHEMISTRY

Major element concentrations of plagioclase and clinopyroxene phenocrysts, as well as plagioclase and clinopyroxene microlites, were measured on a Cameca SX100 electron microprobe at the Open University (UK).

Table 2: Selected plagioclase crystal size distribution input and output data

Sample	Aspect ratio	Vol. phase prop. (%)	No. of crystals	L_{max} (mm)	Slope	ln(n_0)	Ci (mm)	Ci_{100} (mm)	Q
XBS-89 microlites	1:3·9:9·5	48	338	0·69	3·69	6·81	1·41	2·96	0·5945
XBS-89 inclusion (1)	1:1·5:2·8	61	260	2·69	1·52	2·16	1·89	3·10	$6{\cdot}69 \times 10^{-6}$
XBS-89 inclusion (2)	1:1·9:2·9	59	680	7·23	1·28	1·05	3·76	6·37	1×10^{-12}
XBS-89 inclusion (3)	1:2·1:2·6	55	303	3·5	2·97	3·42	1·08	1·96	0·0002
XBS-128 inclusion (1)	1:1·25:2·3	59	500	4·69	1·33	1·22	4·04	6·85	0·0169
XBS-128 inclusion (2)	1:1·3:2·2	64	265	3·88	1·28	0·96	5·57	8·71	0·0810
XBS-128 inclusion (3)	1:1·4:2·3	31	233	4·05	1·32	0·25	10·37	33·43	0·3291
XBS-279 inclusion	1:1·3:2·3	70	237	4·73	1·26	1·54	4·02	5·74	0·1261
XBSa inclusion (1)	1:1·5:2·6	50	157	4·75	0·93	0·60	8·51	17·02	0·5407
XBSa inclusion (2)	1:1·7:3·2	73	226	2·64	1·19	1·16	7·58	10·38	0·9236
PBD phenocrysts	1:5·0:5·0	22	262	14·12	0·56	4·02	0·18	0·85	0·6750

Aspect ratios calculated using CSDSlice (Morgan & Jerram, 2006). L_{max} corresponds to the average of the four largest crystal lengths measured within a sample.

Analytical conditions included an acceleration voltage of 20 kV and a beam current of 20 nA. Peak counting times were variable and ranged between 10 and 40 s. A defocused 10 μm beam was used for feldspar to minimize loss of alkalis. Sodium counts were continuously monitored during analysis and generally remained stable over at least twice the measurement time. Relative analytical precision [(standard deviation/mean) × 100] was <2% for Si, Al and Ca, <3% for Na and K, <4% for Ti, <5% for Fe and <10% for Mg, based on repeated analysis of natural and synthetic mineral and glass standards.

In this study, the compositions of the major mineral phases, plagioclase and clinopyroxene, were analysed in samples of the PBD and XBSa. The aim of these measurements was to assess the compositional contrast between groundmass microlites and larger plagioclase phenocrysts and inclusion crystals in the PBD and XBSa, respectively, and to complement the CSD data in determining whether the gabbro inclusion plagioclase crystals in different sheets were of the same population of crystals or not. Several crystals that showed evidence for compositional zoning were closely examined to elucidate whether this was reflected in their intracrystalline compositions. Traverses of between five and 30 points were made across 14 plagioclase phenocrysts (of 2 mm to 1 cm in length) in a sample of the PBD. Approximately 45 spot measurements were made of the compositions of microlites in the same sample of the PBD. Fourteen traverses of plagioclase crystals (between four and 14 points), 20 points in plagioclase microlites and ~50 spot points in the skeletal clinopyroxene microlites were carried out in samples from XBSa.

Mineral chemistry results

Figure 11 summarizes the microprobe data for feldspar and clinopyroxene in the samples analysed (all of the raw data are provided as Supplementary Data in Electronic Appendix 3). Plagioclase phenocrysts in the PBD range in composition from An_{68} to An_{46}. The PBD groundmass microlite compositions overlap to some extent with the more sodic plagioclase phenocrysts, but also extend towards more Na-rich compositions (An_{56}–An_{37}). Cumulus plagioclase in the gabbro inclusions of XBSa shows a similar range of compositions, although more calcic compositions (up to An_{82}) also occur. Plagioclase microlites in the gabbro inclusions show a similar range in An content to those in the PBD (An_{56}–An_{29}), although microlites from both the PBD and XBS have somewhat different compositions from the coarse-grained phenocrysts and the plagioclase in the inclusions (Fig. 11a). Microprobe traverses of the optically zoned plagioclase crystals in the PBD and gabbro inclusions (XBSa) reveal discrete major element chemical zonation, with inter-crystal zonation of up to 20 An mol % observed, although the compositional variation across plagioclase zones is typically much less. However, no consistent patterns of plagioclase zoning were observed between the PBD and XBSa. The most significant compositional zoning is observed in plagioclase crystals from the XBSa, rather than the PBD. In the PBD phenocrysts, orthoclase-rich alkali feldspar was identified (Fig. 11a), occupying fractures in plagioclase phenocrysts and around phenocryst edges. The close spatial association of the alkali feldspar with quartz in these settings suggests that the K-feldspar is also the product of secondary alteration. Plagioclase chemical data from the Centre 3 Sithean Mor

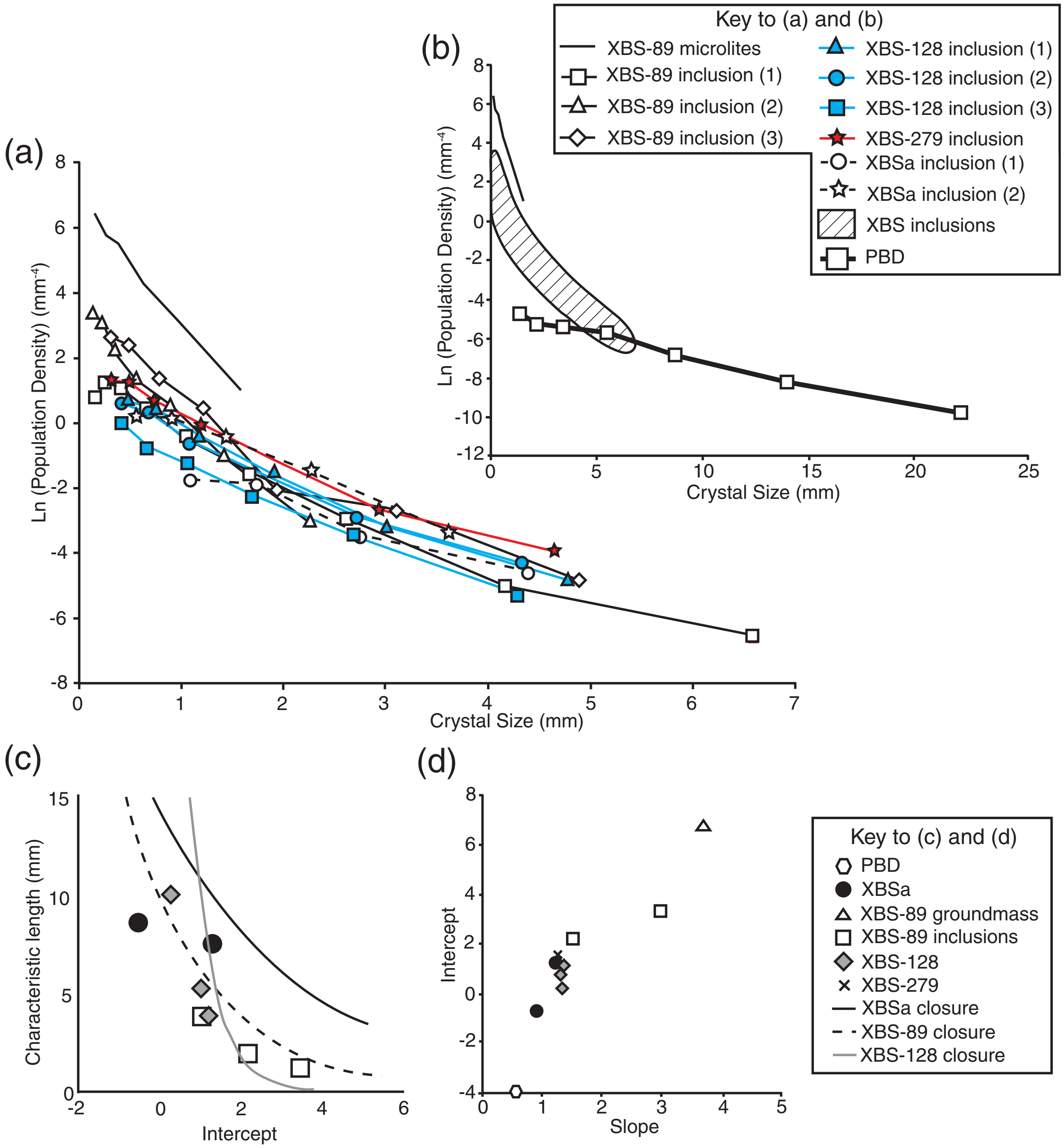

Fig. 10. CSD data for plagioclase crystals from (a) all samples except PBD and (b) all samples. (c) Characteristic length vs intercept plot for the inclusions, as more than one sample was measured for each, with the calculated closure limits. Closure limits, defined by the characteristic length for a volumetric abundance of 100% (Ci_{100}), are calculated after Higgins (2006*b*). (d) Intercept vs slope plot after Zeig & Marsh (2002).

laminated gabbros (O'Driscoll *et al.*, 2008) and plagioclase phenocrysts in some inclined sheets (Geldmacher *et al.*, 1998) are provided for reference in the feldspar ternary diagram, highlighting the compositional similarity in An content to the cumulus plagioclase in the PBD and XBSa, respectively (Fig. 11b). As illustrated in a plot of FeO (wt %) vs An content (mol %) (Fig. 11b), the plagioclase from the Centre 3 Sithean Mor gabbros (O'Driscoll *et al.*, 2008) is characterized by systematically lower FeO contents. In contrast, the plagioclase phenocrysts in some of the inclined sheets (Geldmacher *et al.*, 1998) overlap with those in the PBD and gabbro inclusions, in which FeO contents between 0·4 and 1·2 wt % predominate. FeO contents greater than 1·5 wt % are occasionally preserved in plagioclase microlites in the PBD (Fig. 11b).

Clinopyroxene phenocrysts and microlites in the gabbro inclusions in XBSa are augitic in composition (Fig. 11c), with Mg# $[(Mg \times 100)/(Mg + Fe^{2+})]$ values,

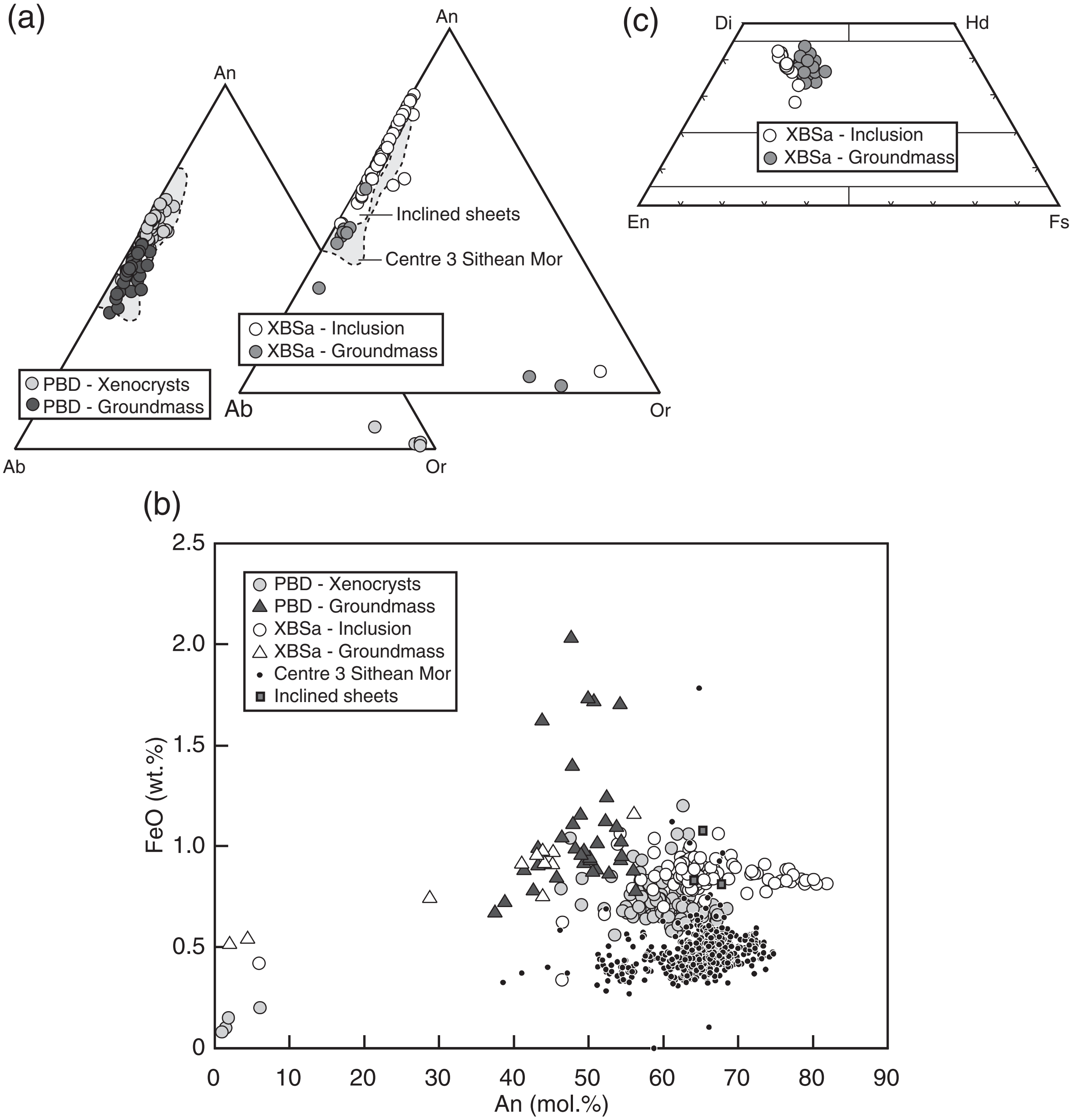

Fig. 11. (a) Compositions (Ab–An–Or) of feldspar phenocrysts and groundmass microlites in the PBD and gabbro blocks. Fields for plagioclases from Centre 3 Sithean Mor (O'Driscoll *et al.*, 2008) and inclined sheets (Geldmacher *et al.*, 1998) are shown for comparison. (b) Plot of FeO (wt %) vs An (mol %) for all plagioclases. The lower FeO contents of the Centre 3 Sithean Mor plagioclases compared with those from the PBD and gabbro blocks should be noted. (c) Compositions (Wo–En–Fs) of clinopyroxene phenocrysts and groundmass microlites in the gabbro blocks. Field boundaries are from Morimoto (1988).

TiO_2 and Al_2O_3 contents in the range of 59–80, 0·5–1·3 wt % and 1·4–3·2 wt %, respectively (Supplementary Data: Electronic Appendix 3). In general, the groundmass microlites ($Wo_{28–43}$, $En_{46–49}$, $Fs_{13–22}$) are more Mg-rich (and Fe-poor) than the phenocrysts ($Wo_{34–44}$, $En_{38–43}$, $Fs_{18–25}$).

DISCUSSION

Mechanisms of sheet emplacement

Determining the magma source location and ascent pathways of sheet intrusions can provide important constraints on the timing and origin of inclusion entrainment. Richey & Thomas (1930) originally interpreted the inclusions in

XBSa as resulting from the *in situ* fragmentation of an early dyke by a subsequent sheet intrusion. Although the XBSa geometry was probably controlled by pre-existing host-rock weaknesses, as suggested by the ramp-flat morphology (Kavanagh *et al.*, 2006; Burchardt, 2008; Menand, 2008), it is likely that the inclusions do not represent a brecciated pre-existing dyke *sensu* Richey & Thomas (1930). Instead, the coarse grain size and framework texture of the gabbro inclusions suggests that they originally developed through crystallization and accumulation processes associated with cumulate development in an upper crustal magma chamber. The pronounced difference between plagioclase microlites and cumulus plagioclase populations, evidenced in the XBS-89 by variable CSD slopes (Fig. 10a) and in the PBD and XBSa by geochemical variations (Fig. 11a), suggests that the inclusion-bearing sheet magma and the inclusions are not cognate. This implies that the gabbro inclusions were entrained and transported from a separate source(s) compared with the host magma. To elucidate the source of the gabbro inclusions, the magmatic pathways of the host sheet intrusions first need to be reconstructed.

Magma source of the PBD and XBS

Rock magnetic experiments reveal that a multidomain low-Ti titanomagnetite phase dominates the magnetic mineralogy of the XBSa and PBD. Given the intrinsically high magnetic susceptibility of magnetite, this dominance implies that the contribution of Fe-sulphides (e.g. PBD-1L) or Fe–Mg silicates to the magnetic fabric is negligible (Tarling & Hrouda, 1993). All magnetic fabrics can therefore be considered to reflect the shape-preferred orientation of the groundmass titanomagnetite grains (Hrouda, 1982; Rochette *et al.*, 1992; Bouchez, 1997, 2000). Although the Lowrie–Fuller test and the IRM acquisition experiments identify the presence of very minor populations of single-domain and pseudo-single-domain grain sizes in the gabbro inclusions, the dominance of the multidomain titanomagnetites suggests that most AMS fabrics are 'normal'. This is consistent with the magnetic lineations and foliation planes, which are consistently oriented subparallel to the intrusion plane with K_1 often close to the intrusive sheet dip azimuth (Figs 2 and 4). Magnetic fabrics measured from within the gabbro inclusions are principally carried by the host magma groundmass, which has an overall modal abundance of 20–40 vol. % and dominates the interstitial component of the inclusions. Variability in the magnetic mineralogy of the gabbro inclusions with respect to the external host groundmass is interpreted to reflect mixing of the host groundmass with a primary gabbro signature. The dominance of prolate fabrics in XBS-89 and the absence of significant evidence for post-intrusion deformation or textural equilibration suggest that the preserved groundmass magnetic fabrics are primary and probably reflect magma flow patterns.

Several XBS-89 samples (Fig. 4) display magnetic foliations that are oblique or perpendicular to the intrusion plane (i.e. XBS-89.1, XBS-89.2, XBS-89.5, XBS-89.6, XBS-89.7, XBS-89.10), a feature commonly associated with inverse fabrics (Rochette *et al.*, 1999; Ferré, 2002). The development of an inverse fabric implies that all principal susceptibility axes are incorrect, which is inconsistent with the observed parallelism among the XBS-89 K_1 lineations. A more likely explanation for the anomalous magnetic foliations may be that the magnetic fabric is intermediate, where the K_2 and K_3 axes of a normal prolate fabric have been reversed by a small proportion (~20 vol. % of the Fe–Ti oxide population) of prolate single-domain magnetites (see Ferré, 2002). This would result in K_2 being situated towards the centre of the equal-area stereographic projection, on which the AMS data are displayed, similar to the position of K_3 in the normal magnetic fabrics of XBS-89 (i.e. XBS-89.3, XBS-89.4, XBS-89.8 and XBS-89.9; Fig. 4). However, there is no significant reduction in K_{mean} (except perhaps for XBS-89.10), compared with the normal fabrics, as is predicted for intermediate fabrics (see Ferré, 2002). Importantly, the K_1 lineation remains unchanged and may still be used to infer primary magma flow vectors (Fig. 4). Dip-parallel magnetic lineations measured in the XBS and PBD are consistent with a magma reservoir down-dip, probably an upper crustal magma reservoir component of the Ardnamurchan Central Complex (Richey & Thomas, 1930).

Volcanotectonic setting

Although the PBD and PBD-like intrusions are older than the XBS, the consistency in the magma flow patterns as well as the petrological and compositional similarities of the groundmass suggest that the PBD and XBS may originate from the same source. Throughout the evolution of the Ardnamurchan Central Complex, sheet intrusions were emplaced successively (Richey & Thomas, 1930) in a range of orientations dependent on the ambient stress regime. Subvertical regional dykes, striking NW–SE, were emplaced during periods of NE–SW regional extension with little or no influence from a local stress field (Speight *et al.*, 1982; England, 1988). By contrast, phases of increased local compression, where σ_1 was radially inclined inwards and either σ_2 or σ_3 was subhorizontal and concentric, favoured the formation of radial dykes and inclined sheets (Richey & Thomas, 1930; Anderson, 1936; England, 1988; Day, 1989). The observed cross-cutting relationships and strike variations of the sheet intrusions studied here imply emplacement across numerous phases of volcano evolution. The disposition of the PBD and XBS relative to the Ardnamurchan Central Complex includes north–south-striking radial intrusions (i.e. PBD, XBSa and XBSb) and oblique to tangential sheets (i.e. XBS-89, XBS-128, XBS-279) that are subparallel to the local inclined sheet swarms. This variation suggests that sheet emplacement and consequently entrainment of the gabbro inclusions occurred during separate phases of local compression, defined by the alternation of σ_2 (i.e. inclined sheets) or σ_3 (i.e. radial dykes) as the subhorizontal and concentric principal stress axes (Walker, 1993). Changes in the principal stress axis directions were probably related to the growth dynamics of major intrusions within the Ardnamurchan Central Complex (Day, 1989; Walker, 1993; Chadwick & Dieterich, 1995). Overall, it appears plausible that the PBD and XBS sheets were intruded from a central source, over a relatively long time period, and entrained the gabbro inclusions from a shallower level magma reservoir.

Gabbro inclusion crystallization history and provenance

Entrainment of the gabbro inclusions probably occurred when centrally fed sheets (i.e. sheet intrusions originating from within the Ardnamurchan Central Complex) interacted with either one or several, shallow-level crystallizing magma chambers. For many igneous rocks, CSD variations are interpreted to primarily reflect differences in cooling rates (Marsh, 1988, 1998; Zeig & Marsh, 2002; Higgins, 2006*b*), which may allow relative source locations to be evaluated. Quantitative examination of the textures observed within the XBS inclusions reveals a clustering of plagioclase CSD population densities (Fig. 10a) within the different host sheet intrusions, implying that initial crystal accumulation and growth of the cumulate plagioclase occurred within a similar cooling regime. Given the limited areal extent of the XBS (Fig. 1) and the petrological similarity between the gabbro inclusions, it is therefore likely that the gabbro inclusions were entrained from a single source reservoir, and have undergone only minor textural modification in transit.

A genetic link may tentatively be proposed for the PBD and XBS plagioclase cargoes, based on the overlap (>50%) in plagioclase chemical compositions for the phenocrysts and the plagioclase-rich inclusions (Fig. 11). Figure 10d suggests that the coarse-grained, euhedral PBD plagioclase phenocrysts probably grew in the interior of a magma chamber while the XBS cumulus plagioclase crystals cooled more quickly, plausibly closer to the magma chamber margin (see Zeig & Marsh, 2002). This suggests that two distinct crystal populations have been entrained. Alternatively, the PBD phenocrysts may originate from a different source within the Ardnamurchan Central Complex that was broadly similar in plagioclase composition to that of the XBS gabbro inclusions.

The dip-parallel magma flow pattern within the PBD and XBS suggests that the inclusions originated from a point roughly subjacent to their present outcrop location. The closest exposed major intrusion and potential source for the gabbro inclusions is the laccolithic Marginal Border Group of the Hypersthene Gabbro (Fig. 1b), which crops out ~1 km to the north of the XBS (Day, 1989). Extrapolation of the shallow, southward dipping (15°) upper contact (i.e. assuming it is planar) of the laccolith suggests it should lie about 200 m below the current outcrop range of XBS. This reconstruction is supported by the measured extension of gravity and aeromagnetic anomalies offshore the south coast of Ardnamurchan (Emeleus, 2009). Texturally, the plagioclase populations of the Hypersthene Gabbro (Wells, 1953), specifically the augite-troctolite facies of Day (1989) and the gabbro inclusions (this study), are very similar with both displaying tabular, euhedral crystals ranging from 1 to 10 mm in length. Whereas the augite-troctolite facies is restricted to small areas at Beinn na Seilg and Glebe Hill (Fig. 1a), several adjacent inclined sheets at Glebe Hill contain presumed cumulus plagioclase phenocrysts often displaying resorption textures and glomerocrysts containing subophitic clinopyroxene (Day, 1989). The anorthite content of the plagioclase measured from the PBD (An_{56}–An_{37}) and XBSa (An_{56}–An_{29}) also overlaps with the range determined by Wells (1953) for the Hypersthene Gabbro (An_{76}–An_{20}). Given the close proximity and textural similarities, it is probable that the gabbro inclusions originated from an unexposed augite-troctolite facies located towards the margin (Fig. 10d) of the Hypersthene Gabbro.

Compositional zoning and resorption textures in gabbro inclusion plagioclase and clinopyroxene (Fig. 6c, e and f) are predominantly observed towards the outer edge of the inclusions, consistent with a state of chemical disequilibrium with the host sheet magma. This suggests that any assimilation and textural equilibration of the gabbro inclusions was localized and did not affect the core of the larger gabbro inclusions (i.e. >10 cm in diameter). Therefore, it is most likely that the composition and framework texture of the gabbro inclusion interiors is primary. The absence of resorption textures in clinopyroxene crystals containing unzoned plagioclase chadacrysts, observed in the cores of the gabbro inclusions, supports this interpretation (Fig. 6d). The low plagioclase–plagioclase–clinopyroxene apparent dihedral angles and preservation of impingement textures in gabbro inclusion centres (see Holness *et al.*, 2005) suggest little subsolidus modification of their original igneous microstructure and entrainment from a crystal-mush zone prior to or soon after solidification.

Transport and fluid dynamics of the gabbro inclusions and sheet intrusions

The rheological behaviour of magma strongly controls its flow dynamics (e.g. velocity profile and whether flow is laminar or turbulent; Spera, 1980) as well as the transport and distribution of inclusions (Sparks *et al.*, 1977). Flow of basaltic magma within planar conduits is typically suggested to behave as either a Newtonian or a Bingham fluid (Sparks *et al.*, 1977; Correa-Gomes *et al.*, 2001; Callot & Guichet, 2003), depending on whether the suspended crystal content exceeds ~35 vol. % (Féménias *et al.*, 2004; Yamato *et al.*, 2011). In contrast to Newtonian fluids, which may flow regardless of the applied stresses, Bingham fluids are viscoplastic and behave as a solid at low stresses but as a viscous fluid once a critical yield stress has been overcome (Twiss & Moores, 2007). Increasing the crystal content of a magma, either rapidly or progressively, may therefore result in the transition to Bingham behaviour (Yamato *et al.*, 2011) with a consequent decrease in velocity and increase in viscosity. An important implication of this transition may be observed in the schematic magma-velocity gradient profiles in Fig. 12a (Correa-Gomes *et al.*, 2001; Yamato *et al.*, 2011). In both cases, the velocity gradient is greatest at the conduit margins owing to the frictional drag imparted by the wall-rocks and least in the sheet core (Fig. 12a; Correa-Gomes *et al.*, 2001). There are several pertinent petrological observations and AMS measurements from the inclusion-bearing sheets that may be utilized to elucidate magmatic conditions during gabbro inclusion transport on Ardnamurchan.

Magma rheology prior to gabbro inclusion entrainment

The gabbro inclusions and host-rock xenoliths (e.g. in XBS-89) observed often appear to be restricted to particular magmatic segments, despite the coalesced nature of the sheets (e.g. Figs 2 and 4). With the exception of subtle variations in grain size, the groundmasses of the PBD and XBS are similar and contain fine-grained, equigranular skeletal microlites of plagioclase, clinopyroxene and titanomagnetite. This implies that separate sheets and their component magmatic segments identified from field observations of intrusive step and broken bridge positions (Figs 2 and 4) have similar crystallization histories. Magmatic segments that do not contain gabbro inclusions (or host-rock xenoliths) may therefore potentially be used as a proxy to determine the initial magma flow dynamics of the sheet intrusions. Given the absence of phenocrysts in the inclusion-free sheet segments, it is probable that the initial crystal content of the magma was low (~<10 vol. %) and that it probably behaved as a Newtonian fluid (Yamato *et al.*, 2011). The consistent AMS fabrics oriented within the plane of intrusion further suggest that the magma flow was laminar. From the average half-width (h) of the XBS conduits (0·58 m) the approximate Reynolds number (Re) of the magma may be calculated (Wartho *et al.*, 2001; Holness & Humphries, 2003):

$$\mathrm{Re} = [(\Delta P/z)(h^3/\mu^2)\rho_1]^{2/3}.$$

Here, we assume that the sheet magma had a typical density ($\rho_l = 2650\ \mathrm{kg\ m^{-3}}$), dynamic viscosity ($\mu = 146$ Pa s) and a minimum driving pressure ($\Delta P/z$) of 3146 Pa m^{-1}. The driving pressure was calculated using the method described by Wartho *et al.* (2001) and assumes a maximum magma source depth of 4 km (i.e. 3 km beneath the current surface; Emeleus & Bell, 2005; Magee *et al.*, 2012*a*) and an average overburden density of 3000 kg m^{-3}. The calculated minimum Re value of 63 supports a laminar magma flow regime ($<1{\cdot}3 \times 10^3$) and is consistent with the findings of Holness & Humphries (2003), who showed that turbulent flow is probably restricted to conduits with half-widths >4 m. Using the same parameters, the minimum mean magma velocity (u_m) prior to entrainment is calculated to be ~3 m s^{-1} (Holness & Humphries, 2003):

$$u_\mathrm{m} = (\Delta P/z)(h^2/3\mu).$$

It is important to note that although the driving pressure value used here is only speculative (see Holness & Humphries, 2003), it provides a useful constraint (i.e. assuming driving pressure remains constant) for comparing the relative differences in rheological behaviour of the magma prior to and after inclusion entrainment.

Magma rheology and flow post-entrainment

The magnetic fabrics of samples collected from the host sheet groundmass and from the outer margins of gabbro inclusions are coaxial (i.e. fabric orientations are subparallel). As there is little evidence in the XBS of post-emplacement deformation and many of the fabrics are prolate, we suggest that coaxial magnetic fabrics developed simultaneously during intrusion (see Hrouda *et al.*, 1999; Yoshinobu *et al.*, 2009). Because the magnetic fabrics within the gabbro inclusions are carried by the infiltrated groundmass around the inclusion edges, coaxial fabrics may be generated by the flow of magma through the gabbro inclusions. This implies that the magma velocity would have been greater than the transport velocity of the inclusions, requiring the magma flow to wrap around the inclusions. However, the magnetic fabric patterns indicate that magma flow did not wrap around the inclusions and instead suggests that the magma and inclusions travelled at equal velocities with any infiltrated magma remaining in the interstitial pore spaces. The generation of an emplacement-related fabric within the gabbro inclusions therefore implies that the deviatoric stress associated with magma flow was transmitted into the gabbro inclusions and influenced the orientation of growing titanomagnetite crystals within the locally infiltrated groundmass; a process that Hrouda *et al.* (1999) and Yoshinobu *et al.* (2009) highlighted, which requires a host magma with a yield strength (i.e. a Bingham rheology). A Bingham rheology would also explain the relatively consistent AMS strength and shape magnitudes measured throughout the PBD and XBS, a relationship often interpreted as evidence of a strong similarity in melt and inclusion viscosity (Hrouda *et al.*, 1999; Yoshinobu *et al.*, 2009). The minimum yield strength of a Bingham fluid (magma) required to entrain the largest gabbro inclusions (75 cm width) with an excess density of ~130 kg m^{-3}, assuming a typical basalt magma density (ρ_l) of 2650 kg m^{-3} and a maximum inclusion density (ρ_m; 2780·5 kg m^{-3}) consisting of 60 vol. % plagioclase crystals (2730 kg m^{-3}), 15 vol. % intercumulus clinopyroxene (~3200 kg m^{-3}) and 25 vol. % of the host magma, is <200 N m^{-2} (Fig. 12b; Sparks *et al.*, 1977; Yoshinobu *et al.*, 2009). This is consistent with the yield strength values presented by Sparks *et al.* (1977).

Magma is generally considered to change from a Newtonian to a Bingham rheology when its crystallinity reaches ~35 vol. % (Féménias *et al.*, 2004). This implies either that the gabbro inclusions in the XBS were entrained towards the end of the intrusion phase (i.e. ~35% of the fine-grained groundmass had crystallized) or that the actual entrainment of the inclusions promoted the magma to behave as a Bingham fluid. Regardless, calculating the minimum settling velocities for the inclusions in Newtonian and Bingham fluids using Stokes' Law (and a modified version thereof) may provide some insights into the relative changes in transport dynamics. Assuming the host magma continues to behave as a Newtonian fluid during inclusion transport, average-sized (radius *r* of 0·2 m; crystallinity of 45%) gabbro inclusions are calculated to settle (V_0) at 0·0028 m s^{-1}, whereas the largest inclusion in XBSa (*r* of 0·38 cm; crystallinity of 75%) should settle at 0·028 m s^{-1} (Morin & Corriveau, 1996):

$$V_0 = \left[2g\left(r^2\right)\right](\rho_m - \rho_l)/90\mu$$

where *g* is gravitational acceleration (9·81 m s^{-2}) and μ is the dynamic viscosity (146 Pa s). These minimum inclusion settling velocities (V_0), which provide an estimation of the minimum magma ascent velocity (i.e. $u_m > V_0$ as the inclusions have been transported upwards; Spera, 1980), are up to three orders of magnitude slower than the calculated pre-entrainment magma velocities. To calculate the minimum settling velocities of inclusions in a Bingham magma (V), Stokes' Law has to be modified to incorporate the solid fraction (F) to simulate the yield strength (Morin & Corriveau, 1996):

$$V = V_0(1 - F)^{4\cdot65}.$$

A maximum solid fraction of 0·5 is utilized, assuming the gabbro inclusions (~75 vol. % crystallinity) account for on average 75% of the current sheet volume. The calculated V values of 0·0003 m s^{-1} (average inclusion size) and 0·001 m s^{-1} (largest inclusion) are an order of magnitude lower than their respective settling velocities in a Newtonian fluid. Although these results do not preclude a Newtonian or Bingham magma from travelling at similar velocities to each other, several studies (e.g. Morin & Corriveau, 1996) have shown that an increase in the effective crystallinity of sheet intrusions associated with inclusion and xenolith entrainment often reduces mean magma velocity. Characterization of the post-entrainment magma as a Newtonian fluid therefore probably overestimates the minimum settling velocities of the gabbro inclusions.

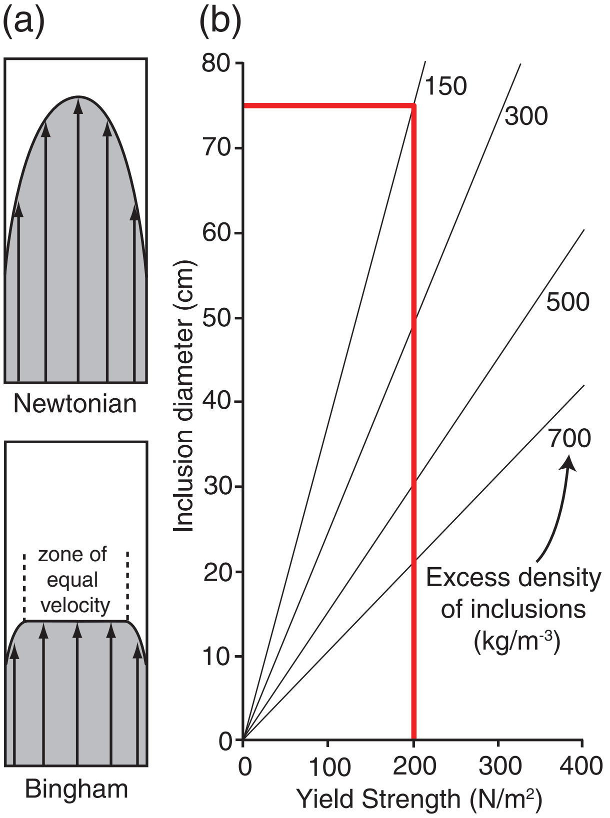

Fig. 12. (a) Schematic magma-velocity profiles for Newtonian and Bingham behaviour (after Correa-Gomes *et al.*, 2001). (b) The calculated minimum yield strength (bold line) required for a Bingham magma to entrain gabbro inclusions, derived from a crystal-mush, 75 cm in diameter (modified from Sparks *et al.*, 1977; Yoshinobu *et al.*, 2009).

Distribution of gabbro inclusions within the XBS

The rheological behaviour of magma is an important control on xenolith distribution throughout intrusions (Nkono *et al.*, 2006). Sheet intrusions initially propagate as thin discrete segments that coalesce through inflation (Rickwood, 1990; Hutton, 2009). The presence of gabbro inclusions less than 75% the width of the host sheet intrusions implies significant inflation and probably segment coalescence prior to entrainment. Restriction of the gabbro inclusions to relict segments indicates either that specific sections of the sheet intrusions interacted with the inclusion source or that the magma dynamics of specific segments allowed entrainment. Although a rheological transition to a Bingham behaviour (i.e. through increasing the effective crystallinity) promotes further inclusion entrainment, owing to the increased viscosity (Sparks *et al.*, 1977), it does not explain how some originally Newtonian magma segments entrained inclusions whereas others did not. It is most likely that inclusion distribution within single sheets therefore reflects a primary spatial relationship between the magmatic pathways and the inclusion source position.

Within the inclusion-bearing segment of XBS-89, the gabbro inclusions are predominantly contained within a planar zone ~20 cm from the basal contact (Figs 3d, 4 and 13). Similarly, host-rock sandstone and basalt xenoliths accumulated ~10–20 cm from the top contact of XBS-89 (Fig. 13). The planar distribution of the inclusions and xenoliths, parallel to the intrusive contacts, is consistent with a laminar magma flow regime. The vertical separation of the distinct inclusion and xenolith lithologies possibly relates to the inherent density contrast with the host magma, where the lighter xenoliths (i.e. the sandstone and basalt host-rocks) 'float' and the denser gabbro inclusions 'sink' (Holness & Humphries, 2003). It is interesting to note that the planar zones of inclusion and xenolith accumulation do not occur at the intrusion contacts. Considering a Bingham magma rheology, two plausible alternatives are considered that may account for this distribution. (1) During sheet inflation and the transition from Newtonian to Bingham behaviour, the solidification front continuously progresses inwards from the sheet margins. The accumulation of inclusions and xenoliths ~20 cm from the intrusion–country rock contact may therefore indicate the position of the solidification front (i.e. the pseudo-intrusion margins) following entrainment. (2) Alternatively, given that the greatest magma velocity in Bingham magmas occurs across the majority of the sheet intrusion, density contrasts of the inclusions and xenoliths relative to the host magma, grain dispersal pressures and flow segregation may act to differentiate the lithologies and allow accumulation in planar zones at the transition to peak magma velocity (Figs 12a and 13).

The acquisition of a Bingham rheology within inclusion-bearing magmatic segments implies that there may have been a significant difference, up to four orders of magnitude, in magma velocity and viscosity compared with the inclusion-free Newtonian magmatic segments. From the observed groundmass grain size variations in the XBSa segments and the confined distribution of the gabbro inclusions, we suggest that high velocity gradients developed between the two segments owing to variations in magma rheology restricted lateral mixing and potentially provided zones suitable for inclusion accumulation (Fig. 13). The high abundance of gabbro inclusions surrounding the limestone broken bridge in XBS-128 may reflect this process (Fig. 5a). Holness & Humphries (2003) described a similar division in the internal magma flow dynamics and xenolith distribution within the Traigh Bhàn na Sgùrra Sill on the Isle of Mull. This correlation suggests that one end-member of segment partitioning dependent on the magma dynamics may be the development of internal chill zones (Glazner *et al.*, 2004). Subtle differences in magma rheology, between adjacent segments, may also explain the preservation of primary magmatic fabrics within multiple, discrete magma flow lobes of an otherwise coalesced intrusive body containing no visible internal contacts (e.g. the Trawenagh Bay Granite, Ireland, Stevenson *et al.*,

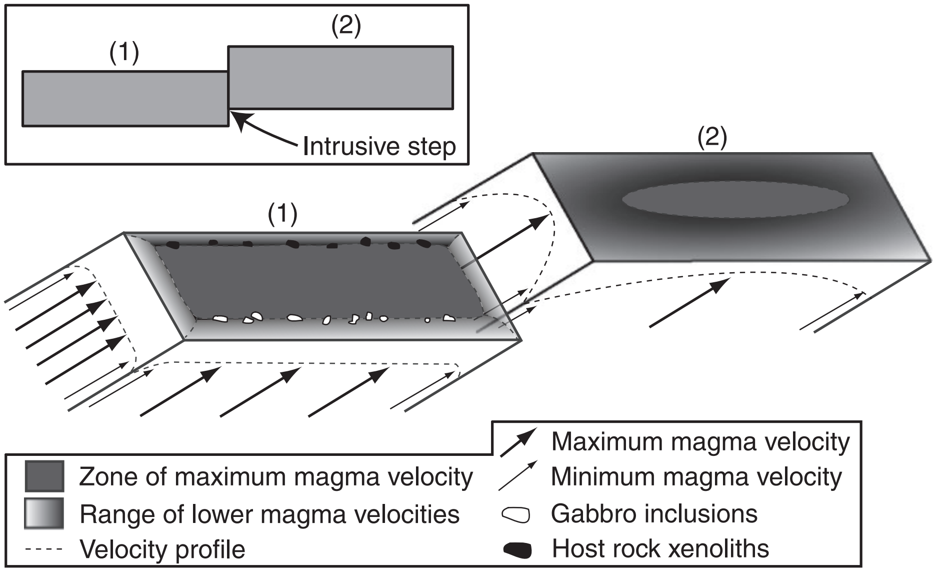

Fig. 13. Sketch of two coalesced magma segments (inset shows a cross-section) characterized by different magma rheologies. Segment (1) behaves as a Bingham fluid, owing to the incorporation of inclusions and xenoliths, whereas segment (2) is crystal-free and acts as a Newtonian fluid. The difference in predicted zones of maximum magma velocity within the two segments should be noted. Although Bingham fluids travel at relatively lower velocities, the zone of maximum magma flow is comparatively larger. Within Bingham fluids, inclusions and/or xenoliths are suggested to accumulate at the boundary of the maximum magma velocity zone; in this case a short distance from the top and basal contacts similar to XBS-89.

2007; the Ben Hiant Dolerite, Ardnamurchan, Magee *et al.*, 2012*b*).

CONCLUSIONS

This study of several areally restricted inclusion-bearing sheet intrusions on Ardnamurchan shows that integrating field and petrological observations with rock magnetic data and mineral chemistry can provide important information on the transport dynamics of sub-volcanic intrusions. Several key conclusions include the following:

(1) Compositional and textural similarities between the groundmass of the separate sheet intrusions suggest that they originate from a similar source and behaved, at least initially, as Newtonian fluids. AMS data reveal sheet dip-parallel magnetic lineations, interpreted as parallel primary magma flow vectors, consistent with a source reservoir down-dip.

(2) The gabbro inclusions and cumulus plagioclase phenocrysts of the XBS and PBD, respectively, are not cognate with the host intrusion magma. It is probable that the host sheet intrusions entrained the cumulus plagioclase cargoes from the southern extension of the major Hypersthene Gabbro intrusion, located ~200 m below the present surface, during ascent. The limited areal extent of the XBS and PBD intrusions may correlate with a small inclusion source zone within the Hypersthene Gabbro, possibly a lens of augite-troctolite.

(3) Petrographical observations reveal that during inclusion transport, the host sheet magma infiltrated the inclusions following localized assimilation and disaggregation of the inclusion adjacent to the outer edges.

(4) Entrainment of the gabbro inclusions instigated or resulted from a transition from Newtonian to Bingham magma behaviour. This probably corresponded to a consequent decrease in magma velocity and increase in viscosity, which aided inclusion transport.

(5) Within single sheets, the gabbro inclusions are often laterally restricted to discrete segments despite an overall sheet coalescence. This is interpreted to reflect the limited interaction of only certain magmatic segments with the inclusion source. The inherent change in magma rheology, associated with inclusion entrainment, probably produced a high velocity gradient between segments that prevented lateral magma mixing and inclusion transport.

ACKNOWLEDGEMENTS

The cored drill-holes produced over the course of this study were subsequently infilled under the guidance of Scottish National Heritage. Andy Tindle is thanked for assistance using the electron microprobe at The Open University. Marian Holness, Sandy Cruden, Fiona Meade, Bruce Marsh and John Geissman are thanked for insightful and constructive reviews of this paper. We are also grateful to John Gamble for helpful editorial handling.

FUNDING

C.M. acknowledges funding through a Natural Environment Research Council PhD studentship (NER/S/A/2008/85478). B.O'D acknowledges support from a University College Dublin Seed Funding Grant whilst formerly at UCD.

SUPPLEMENTARY DATA

Supplementary data for this paper are available at *Journal of Petrology* online.

REFERENCES

Anderson, A. T. (1976). Magma mixing: petrological process and volcanological tool. *Journal of Volcanology and Geothermal Research* **1**, 3–33.

Anderson, E. M. (1936). Dynamics of formation of cone-sheets, ring-dikes, and cauldron subsidence. *Proceedings of the Royal Society of Edinburgh* **56**, 128–157.

Archanjo, C. J., Launeau, P. & Bouchez, J. L. (1995). Magnetic fabric vs. magnetite and biotite shape fabrics of the magnetite-bearing granite pluton of Gameleiras (Northeast Brazil). *Physics of the Earth and Planetary Interiors* **86**, 63–75.

Aubourg, C., Giordano, G., Mattei, M. & Speranze, F. (2002). Magma flow in sub-aqueous rhyolitic dikes inferred from magnetic fabric analysis (Ponza Island, W. Italy). *Physics and Chemistry of the Earth* **27**, 1263–1272.

Blake, S. & Fink, J. H. (2000). On the deformation and freezing of enclaves during magma mixing. *Journal of Volcanology and Geothermal Research* **95**, 1–8.

Boorman, S., Boudreau, A. & Kruger, F. J. (2004). The Lower Zone–Critical Zone transition of the Bushveld Complex: a quantitative textural study. *Journal of Petrology* **45**, 1209–1235.

Borradaile, G. J. (1987). Anisotropy of magnetic susceptibility: rock composition versus strain. *Tectonophysics* **138**, 327–329.

Bouchez, J. L. (1997). Granite is never isotropic: an introduction to AMS studies of granitic rocks. In: Bouchez, J. L., Hutton, D. H. W. & Stephens, W. E. (eds) *Granite: from Segregation of Melt to Emplacement Fabrics.* Dordrecht: Kluwer, pp. 95–112.

Bouchez, J. L. (2000). Anisotropie de susceptibilité magnétique et fabrique des granites. *Comptes Rendus de l'Académie des Sciences* **330**, 1–14.

Brown, D. J. & Bell, B. R. (2007). Debris flow deposits within the Palaeogene lava fields of NW Scotland: evidence for mass wasting of the volcanic landscape during emplacement of the Ardnamurchan Central Complex. *Bulletin of Volcanology* **69**, 847–868.

Burchardt, S. (2008). New insights into the mechanics of sill emplacement provided by field observations of the Njardvik Sill, Northeast Iceland. *Journal of Volcanology and Geothermal Research* **173**, 280–288.

Callot, J. P. & Guichet, X. (2003). Rock texture and magnetic lineation in dykes: A simple analytical model. *Tectonophysics* **366**, 207–222.

Cañón-Tapia, E. & Chávez-Álvarez, M. J. (2004). Implications for the anisotropy of magnetic susceptibility of dykes. In: Martín-Hernández, F., Lüneburg, C. M., Aubourg, C. & Jackson, M.

(eds) *Magnetic Fabric: Methods and Applications. Geological Society, London, Special Publications* **238**, 227–249.

Cashman, K. V. & Marsh, B. D. (1988). Crystal size distribution (CSD) in rocks and the kinetics and dynamics of crystallisation II: Makaopuhi lava lake. *Contributions to Mineralogy and Petrology* **99**, 292–305.

Chadwick, W. W. & Dieterich, J. H. (1995). Mechanical modelling of circumferential and radial dike intrusion on Galapagos volcanoes. *Journal of Volcanology and Geothermal Research* **66**, 37–52.

Correa-Gomes, L. C., Souza Filho, C. R., Martins, C. J. F. N. & Oliviera, E. P. (2001). Development of symmetrical and asymmetrical fabrics in sheet-like igneous bodies: the role of magma flow and wall-rock displacements in theoretical and natural cases. *Journal of Structural Geology* **23**, 1415–1428.

Cruden, A. R. & Launeau, P. (1994). Structure, magnetic fabric and emplacement of the Archean Lebel Stock, S.W. Abitibi Greenstone Belt. *Journal of Structural Geology* **16**, 1481–1486.

Day, S. J. (1989). The geology of the Hypersthene Gabbro of Ardnamurchan Point and its implications for its evolution as an upper crustal basic magma chamber, PhD thesis, University of Durham.

Dragoni, M., Lanza, R. & Tallarico, A. (1997). Magnetic anisotropy produced by magma flow: theoretical model and experimental data from Ferrar dolerite sills. *Geophysical Journal International* **128**, 230–240.

Dunlop, D. J. & Özdemir, O. (1997). *Rock Magnetism: Fundamentals and Frontiers. Cambridge Studies in Magnetism, 3.* New York: Cambridge University Press.

Emeleus, C. H. (2009). Ardnamurchan Central Complex, bedrock and superficial deposits, 1:25,000 Geology Series, 1 sheet. Keyworth, Nottingham: British Geological Survey.

Emeleus, C. H. & Bell, B. R. (2005). *British Regional Geology: The Palaeogene Volcanic Districts of Scotland*, Fourth edn. Nottingham: British Geological Survey.

England, R. W. (1988). The early Tertiary stress regime in NW Britain: evidence from the patterns of volcanic activity. In: Morgan, A. C. & Parson, L. M. (eds) *Early Tertiary Volcanism and the Opening of the NE Atlantic. Geological Society, London, Special Publications* **39**, 381–389.

Féménias, O., Diot, H., Berza, T., Gauffriau, A. & Demaiffe, D. (2004). Asymmetrical to symmetrical magnetic fabric of dikes: Paleo-flow orientations and paleo-stresses recorded on feeder-bodies from the Motru Dike Swarm (Romania). *Journal of Structural Geology* **26**, 1401–1418.

Ferré, E. C. (2002). Theoretical models of intermediate and inverse AMS fabrics. *Geophysical Research Letters* **29**, 31-1–31-4.

Gautneb, H., Gudmundsson, A. & Oskarsson, N. (1989). Structure, petrochemistry and evolution of a sheet swarm in an Icelandic central volcano. *Geological Magazine* **126**, 659–673.

Geldmacher, J., Haase, K. M., Devey, C. W. & Garbe-Schönberg, C. D. (1998). The petrogenesis of Tertiary cone-sheets in Ardnamurchan, NW Scotland: petrological and geochemical constraints on crustal contamination and partial melting. *Contributions to Mineralogy and Petrology* **131**, 196–209.

Genareau, K. & Clarke, A. B. (2010). Heterogeneous clasts as windows into magma mingling at Soufrière Hills volcano. *Geophysical Research Letters* **37**, L00E02.

Glazner, A. F., Bartley, J. M., Coleman, D. S., Gray, W. & Taylor, R. Z. (2004). Are plutons assembled over millions of years by amalgamation from small magma chambers? *GSA Today* **14**, 4–11.

Hargraves, R. B., Johnson, D. & Chan, C. Y. (1991). Distribution anisotropy: the cause of AMS in igneous rocks? *Geophysical Research Letters* **18**, 2193–2196.

Higgins, M. D. (2000). Measurement of crystal size distributions. *American Mineralogist* **85**, 1105–1116.

Higgins, M. D. (2002). A crystal size-distribution study of the Kiglapait layered mafic intrusion, Labrador, Canada: evidence for textural coarsening. *Contributions to Mineralogy and Petrology* **144**, 314–330.

Higgins, M. D. (2006*a*). Verification of ideal semi-logarithmic, lognormal or fractal crystal size distributions from 2D datasets. *Journal of Volcanology and Geothermal Research* **154**, 8–16.

Higgins, M. D. (2006*b*). *Quantitative Textural Measurements in Igneous and Metamorphic Petrology.* Cambridge: Cambridge University Press.

Holness, M. B. & Humphries, M. C. S. (2003). The Traigh Bhàn na Sgùrra Sill, Isle of Mull: Flow localization in a major magma conduit. *Journal of Petrology* **44**, 1961–1976.

Holness, M. B., Cheadle, M. J. & McKenzie, D. (2005). On the use of changes in dihedral angle to decode late-stage textural evolution in cumulates. *Journal of Petrology* **46**, 1565–1583.

Holness, M. B., Anderson, A. T., Martin, M. B., Maclennan, J., Passmore, E. & Schwindinger, K. (2007). Textures in partially solidified crystalline nodules: a window into the pore structure of slowly cooled mafic intrusions. *Journal of Petrology* **48**, 1243–1264.

Horsman, E., Tikoff, B. & Morgan, S. S. (2005). Emplacement-related fabric in a sill and multiple sheets in the Maiden Creek sill, Henry Mountains, Utah. *Journal of Structural Geology* **27**, 1426–1444.

Hrouda, F. (1982). Magnetic anisotropy of rocks and its application in geology and geophysics. *Geophysical Survey* **5**, 37–82.

Hrouda, F. (2003). Indices for numerical characterization of the alteration processes of magnetic minerals taking place during investigation of temperature variation of magnetic susceptibility. *Studies in Geophysics and Geodesy* **47**, 847–861.

Hrouda, F., Taborska, S., Schulmann, K., Jezek, J. & Dolejs, D. (1999). Magnetic fabric and rheology of co-mingled magmas in the Nasavrky Plutonic Complex (E Bohemia): implications for intrusive strain regime and emplacement mechanism. *Tectonophysics* **307**, 93–111.

Humphreys, M. C. S., Christopher, T. & Hards, V. (2009). Microlite transfer by disaggregation of mafic inclusions following magma mixing at Soufrière Hills volcano, Montserrat. *Contributions to Mineralogy and Petrology* **157**, 609–624.

Huppert, H. E. & Sparks, R. S. J. (1985). Cooling and contamination of mafic and ultramafic magmas during ascent through continental crust. *Earth and Planetary Science Letters* **74**, 371–386.

Hutton, D. H. W. (2009). Insights into magmatism in volcanic margins: bridge structures and a new mechanism of basic sill emplacement—Theron Mountains, Antarctica. *Petroleum Geoscience* **15**, 269–278.

Irving, E. (1970). The Mid-Atlantic Ridge at 45°N. XIV. Oxidation and magnetic properties of basalt; review and discussion. *Canadian Journal of Earth Sciences* **7**, 1528–1538.

Jelínek, V. (1978). Statistical processing of anisotropy of magnetic susceptibility measured on groups of specimens. *Studies of Geophysics and Geodesy* **22**, 50–62.

Jerram, D. A., Cheadle, M. J. & Philpotts, A. R. (2003). Quantifying the building blocks of igneous rocks: are clustered crystal frameworks the foundation? *Journal of Petrology* **44**, 2033–2051.

Johnson, H. P. & Atwater, T. (1977). A magnetic study of the basalts from the Mid-Atlantic Ridge at 37°N. *Geological Society of America Bulletin* **88**, 637–647.

Johnson, H. P., Lowrie, W. & Kent, D. V. (1975). Stability of anhysteretic remanent magnetisation in fine and coarse magnetite and maghemite particles. *Geophysical Journal of the Royal Astronomical Society* **41**, 1–10.

Kavanagh, J. L., Menand, T. & Sparks, R. S. J. (2006). An experimental investigation of sill formation and propagation in layered elastic media. *Earth and Planetary Science Letters* **245**, 799–813.

Khan, M. A. (1962). The anisotropy of magnetic susceptibility of some igneous and metamorphic rocks. *Journal of Geophysical Research* **67**, 2867–2875.

King, R. F. (1966). The magnetic fabric of some Irish granites. *Geological Journal* **5**, 43–66.

Launeau, P. & Cruden, A. R. (1998). Magmatic fabric acquisition mechanisms in a syenite: Results of a combined anisotropy of magnetic susceptibility and image analysis study. *Journal of Geophysical Research* **103**, 5067–5089.

Lowrie, W. & Fuller, M. (1971). On the alternating field demagnetisation characteristics of multidomain thermoremanent magnetisation in magnetite. *Journal of Geophysical Research* **26**, 6339–6349.

Magee, C., Stevenson, C., O'Driscoll, B., Schofield, N. & McDermott, K. (2012*a*). An alternative emplacement model for the classic Ardnamurchan cone sheet swarm, NW Scotland, involving lateral magma supply via regional dykes. *Journal of Structural Geology* **43**, 73–91.

Magee, C., Stevenson, C. T. E., O'Driscoll, B. & Petronis, M. E. (2012*b*). Local and regional controls on the lateral emplacement of the Ben Hiant Dolerite intrusion, Ardnamurchan (NW Scotland). *Journal of Structural Geology* **39**, 68–82.

Martin, V. M., Pyle, D. M. & Holness, M. B. (2006). The role of crystal frameworks in the preservation of enclaves during magma mixing. *Earth and Planetary Science Letters* **248**, 787–799.

Marsh, B. D. (1988). Crystal size distribution (CSD) in rocks and the kinetics and dynamics of crystallisation I: Theory. *Contributions to Mineralogy and Petrology* **99**, 277–291.

Marsh, B. D. (1998). On the interpretation of crystal size distributions in magmatic systems. *Journal of Petrology* **39**, 553–599.

Marshall, M. & Cox, A. (1972). Magnetic changes in pillow basalts due to sea floor weathering. *Journal of Geophysical Research* **77**, 6459–6469.

Melnik, O. & Sparks, R. S. J. (1999). Nonlinear dynamics of lava dome extrusion. *Nature* **402**, 37–41.

Menand, T. (2008). The mechanics and dynamics of sills in layered elastic rocks and their implications for the growth of laccoliths and other igneous complexes. *Earth and Planetary Science Letters* **267**, 93–99.

Morgan, D. J. & Jerram, D. A. (2006). On estimating crystal shape for crystal size distribution analysis. *Journal of Volcanology and Geothermal Research* **154**, 1–7.

Morimoto, N. (1988). Nomenclature of pyroxenes. *Mineralogical Magazine* **52**, 535–550.

Morin, D. & Corriveau, L. (1996). Fragmentation processes and xenolith transport in a Proterozoic minette dyke, Grenville Province, Quebec. *Contributions to Mineralogy and Petrology* **125**, 319–331.

Moskowitz, B. M. (1981). Methods for estimating Curie temperatures of titanomaghemites from experimental J_s–T data. *Earth and Planetary Science Letters* **53**, 84–88.

Moskowitz, B. M., Jackson, M. & Kissel, C. (1998). Low-temperature magnetic behaviour of titanomagnetites. *Earth and Planetary Science Letters* **157**, 141–149.

Nkono, C., Féménias, O., Diot, H., Berza, T. & Demaiffe, D. (2006). Flowage differentiation in an andesitic dyke of the Motru Dyke Swarm (Southern Carpathians, Romania) inferred from AMS, CSD and geochemistry. *Journal of Volcanology and Geothermal Research* **154**, 201–221.

O'Driscoll, B., Troll, V. R., Reavy, R. J. & Turner, P. (2006). The Great Eucrite intrusion of Ardnamurchan, Scotland: re-evaluating the ring-dyke concept. *Geology* **34**, 189–192.

O'Driscoll, B., Stevenson, C. T. E. & Troll, V. R. (2008). Mineral lamination development in layered gabbros of the British Palaeogene Igneous Province: A combined anisotropy of magnetic susceptibility, textural and mineral chemistry study. *Journal of Petrology* **49**, 1187–1221.

Owens, W. H. (1994). Laboratory drilling of field-orientated block samples. *Journal of Structural Geology* **16**, 1719–1721.

Owens, W. H. (2000). Error estimates in the measurement of anisotropic magnetic susceptibility. *Geophysical Journal International* **142**, 516–526.

Özdemir, O. & O'Reilly, W. (1981). High-temperature hysteresis and other magnetic properties of synthetic monodomain titanomagnetites. *Physics of the Earth and Planetary Interiors* **25**, 406–418.

Özdemir, O. & O'Reilly, W. (1982). Magnetic hysteresis properties of synthetic monodomain titanomaghemites. *Journal of Geomagnetics and Geoelectrics* **34**, 467–478.

Petronis, M. S., Hacker, D. B., Holm, D. K., Geissman, J. W. & Harlan, S. S. (2004). Magmatic flow paths and palaeomagnetism of the Miocene Stoddard Mountain laccolith, Iron Axis region, Southwestern Utah, USA. In: Martín-Hernández, F., Lüneburg, C. M., Aubourg, C. & Jackson, M. (eds) *Magnetic Fabric: Methods and Applications. Geological Society, London, Special Publications* **238**, 251–283.

Polacci, M., Papale, P. & Rosi, M. (2001). Textural heterogeneities in pumices from the climactic eruption of Mount Pinatubo, 15 June 1991, and implications for magma ascent dynamics. *Bulletin of Volcanology* **63**, 83–97.

Potter, D. K. & Stephenson, A. (1988). Single-domain particles in rocks and magnetic fabric analysis. *Geophysical Research Letters* **15**, 1097–1100.

Resmini, R. G. & Marsh, B. D. (1995). Steady-state volcanism, paleoeffusion rates, and magma system volume inferred from plagioclase size distributions in mafic lavas; Dome Mountain, Nevada. *Journal of Volcanology and Geothermal Research* **68**, 273–296.

Richey, J. E. & Thomas, H. H. (1930). *The Geology of Ardnamurchan, North-west Mull and Coll. Memoir of the Geological Survey.* Edinburgh: HMSO.

Rickwood, P. C. (1990). The anatomy of a dyke and the determination of propagation and magma flow directions. In: Parker, A. J., Rickwood, P. C. & Turner, D. H. (eds) *Mafic Dykes and Emplacement Mechanisms*. Rotterdam: A.A. Balkema, pp. 81–100.

Rochette, P., Jackson, M. & Aubourg, C. (1992). Rock magnetism and the interpretation of the anisotropy of magnetic susceptibility. *Review of Geophysics* **30**, 209–226.

Rochette, P., Aubourg, C. & Perrin, M. (1999). Is this magnetic fabric normal? A review and case studies in volcanic formations. *Tectonophysics* **307**, 219–234.

Rutherford, M. J. (2008). Magma ascent rates. In: Putirka, K. D. & Tepley, F. J., III (eds) *Minerals, Inclusions and Volcanic Processes. Mineralogical Society of America and Geochemical Society, Reviews in Mineralogy and Geochemistry* **69**, 241–271.

Sparks, R. S. J. & Marshall, L. A. (1986). Thermal and mechanical constraints on mixing between mafic and silicic magmas. *Journal of Volcanology and Geothermal Research* **29**, 99–124.

Sparks, R. S. J., Pinkerton, H. & MacDonald, R. (1977). The transport of xenoliths in magmas. *Earth and Planetary Science Letters* **35**, 234–238.

Speight, J. M., Skelhorn, R. R., Sloan, T. & Knaap, R. J. (1982). The dike swarms of Scotland. In: Sutherland, D. (ed.) *Igneous Rocks of the British Isles*. Chichester: John Wiley, pp. 449–459.

Spera, F. J. (1980). Aspects of magma transport. In: Hargraves, R. B. (ed.) *Physics of Magmatic Processes*. Princeton: Princeton University Press, pp. 265–323.

Stevenson, C. T. E., Owens, W. H. & Hutton, D. H. W. (2007). Flow lobes in granite: The determination of magma flow direction in the Trawenagh Bay Granite, northwestern Ireland, using anisotropy of magnetic susceptibility. *Geological Society of America Bulletin* **119**, 1368–1386.

Tarling, D. H. & Hrouda, F. (1993). *The Magnetic Anisotropy of Rocks*. New York: Chapman and Hall.

Twiss, R. J. & Moores, E. M. (2007). *Structural Geology*. New York: W. H. Freeman, 736 p.

Uyeda, S., Fuller, M. D., Belshe, J. C. & Girdler, R. W. (1963). Anisotropy of magnetic susceptibility of rocks and minerals. *Journal of Geophysical Research* **68**, 279–91.

Walker, G. P. L. (1993). Re-evaluation of inclined intrusive sheets and dykes in the Cuillins volcano, Isle of Skye. In: Prichard, H. M., Alabaster, T., Harris, N. B. W. & Neary, C. R. (eds) *Magmatic Processes and Plate Tectonics. Geological Society, London, Special Publications* **76**, 489–497.

Walz, F. & Kronmüller, H. (1994). Analysis of magnetic point-defect relaxations in electron-irradiated magnetite. *Physica Status Solidi* **181**, 485–498.

Wartho, J.-A., Kelley, S. P. & Blake, S. (2001). Magma flow regimes in sills deduced from Ar isotope systematics of host rocks. *Journal of Geophysical Research* **106**, 4017–4035.

Wells, M. K. (1953). The structure and petrology of the hypersthene-gabbro intrusion, Ardnamurchan, Argyllshire. *Quarterly Journal of the Geological Society of London* **109**, 367–397.

Yamato, P., Tartese, R., Duretz, T. & May, D. A. (2011). Numerical modelling of magma transport in dykes. *Tectonophysics*, doi:10.1016/j.tecto.2011.05.015.

Yoshinobu, A. S., Wolak, J. M., Paterson, S. R., Pignotta, G. S. & Anderson, H. S. (2009). Determining relative magma and host rock xenolith rheology during magmatic fabric formation in plutons: Examples from the middle and upper crust. *Geosphere* **5**, 270–285.

Žák, J., Paterson, S. R. & Memeti, V. (2007). Four magmatic fabrics in the Tuolumne batholiths, central Sierra Nevada, California (USA): Implications for interpreting fabric patterns in plutons and evolution of magma chambers in the upper crust. *Geological Society of America Bulletin* **119**, 184–201.

Zeig, M. J. & Marsh, B. D. (2002). Crystal size distributions and scaling laws in the quantification of igneous textures. *Journal of Petrology* **43**, 85–101.